Annual Review of Marine Science

Oceanic Frontogenesis

James C. McWilliams

Department of Atmospheric and Oceanic Sciences, University of California, Los Angeles, California 90095-1565, USA; email: jcm@atmos.ucla.edu

Annu. Rev. Mar. Sci. 2021. 13:227–53

The *Annual Review of Marine Science* is online at marine.annualreviews.org

https://doi.org/10.1146/annurev-marine-032320-120725

Keywords

density front, density filament, frontogenesis, secondary circulation, instability, frontal arrest, mixing

Abstract

Frontogenesis is the fluid-dynamical processes that rapidly sharpen horizontal density gradients and their associated horizontal velocity shears. It is a positive feedback process where the ageostrophic, overturning secondary circulation in the cross-front plane accelerates the frontal sharpening until an arrest occurs through frontal instability and other forms of turbulent mixing. Several well-known types of oceanic frontal phenomena are surveyed, their impacts on oceanic system functioning are assessed, and future research is envisioned.

1. INTRODUCTION

Fronts in density ρ and other material concentrations c are common at the oceanic surface, with horizontal widths ℓ from kilometers to meters. A front is defined geometrically as a large gradient in one horizontal direction accompanied by a weak one in the perpendicular horizontal direction (note that the vertical direction is aligned with gravity); i.e., it has a narrow width and an elongated axis following a central isoline of c or ρ along the surface. The evolutionary process of systematic frontal formation and narrowing is called frontogenesis. Frontogenesis is essentially an advective process associated with horizontal gradients in the velocity $\mathbf{u}$. If the frontogenetic advection acts only on a passive concentration c, the sharpening occurs at an at most exponential rate in time (Section 2). However, if the advected quantity is density, then there often is an active, positive feedback on $\mathbf{u}$ through the gravitational force that accelerates the frontogenetic rate through the development of a secondary circulation in the cross-front/vertical plane; in some dynamical approximations, this can lead to an infinitely narrow front in a finite time (Hoskins & Bretherton 1972) (Section 3). In most instances of active frontogenesis, the velocity gradient magnitude $|\nabla \mathbf{u}|$ grows along with $|\nabla \rho|$. Earth's rotation (with Coriolis frequency $f \neq 0$) is a significant dynamical influence in many types of oceanic frontogenesis but not all.

Many observations and measurements have been made of oceanic fronts (e.g., **Figure 1** and Federov 1986), while the theory and modeling literature is smaller and more recent, though rapidly growing. [By contrast, there is an enormous literature on meteorological fronts, with deep roots in the Norwegian school of weather fronts (Bjerknes 1919).] Oceanic fronts can occur everywhere, but they typically are sparsely distributed and well separated from each other. Horizontal wavenumber k spectra for surface temperature T have approximately a k^{-2} shape on scales smaller than the oceanic mesoscales (∼100 km) (Ferrari & Rudnick 2000), which is what would arise from a randomly distributed collection of frontal steps in T. Many of these steps are density

Figure 1

Photograph from across a ship prow of a surface convergence line in the Gulf of Mexico. The line is demarked by floating seaweed. The undulations along its axis are suggestive of a frontal instability. There are also evident differences in the surface gravity waves across the line, indicating local wave–current interaction and perhaps air–sea interaction as well. Photograph by Tamay Ozgokmen, University of Miami.

compensated between T and salinity S, with small ρ differences (Rudnick & Ferrari 1999), but many others are dynamically active with ρ steps. Fronts also occur as elongated, dense filaments (i.e., a ρ maximum over the surface) with sharp gradients at the sides, rather than as a ρ step (McWilliams et al. 2009a). Dynamically active fronts also sharpen the local velocity gradient $\nabla\mathbf{u}$ through the gravity-force feedback on the pressure force, which accelerates both along-front and secondary-circulation (cross-front, usually ageostrophic) currents.

Most fronts in the ocean are transient events with a characteristic life cycle. They arise from preexisting seed gradients, $\nabla\rho$ or ∇c. Frontogenesis occurs when velocity gradients $\nabla\mathbf{u}$ are favorably configured (Section 2). For a passive ∇c, it will continue as long as the alignment persists, until it becomes limited in width at a scale $\ell \sim \sqrt{\kappa/|\nabla\mathbf{u}|}$ in the presence of a horizontal (eddy) diffusivity κ. For dynamically active fronts, with favorable $\nabla\rho$ and $\nabla\mathbf{u}$ alignments, frontogenesis will proceed until the alignment is disrupted or a frontal instability arises and provides cross-frontal density and momentum eddy fluxes that arrest further sharpening (unless some κ associated with a different process becomes limiting first). After frontal arrest, the fronts weaken and decay or their patterns become shredded at a rate dependent on how variable the neighboring currents are.

This review is organized as follows. Simple frontogenetic kinematics are analyzed in Section 2. The dynamical theory and modeling of fronts are presented in Section 3. A survey of frontal phenomena of various types is made in Section 4, organized by climatological, deformation, submesoscale, gravity, topographic, vertical-mixing, and estuarine fronts, plus frontal air–sea interaction—but this is unavoidably an incomplete list. Conclusions are in Section 5.

The approach in this review is fluid dynamical, with the assumption of an incompressible mass balance that precludes shock waves. There are many biological consequences for surface fronts, mainly due to the secondary circulations that transport materials vertically and concentrate buoyant materials along surface convergence lines (Mahadevan 2016), but this topic is not considered here.

2. KINEMATICS

Before examining the fluid dynamics of frontogenesis, first consider the kinematics of conservative passive tracer advection of a dissolved concentration c,

$$\frac{\mathrm{D}c}{\mathrm{D}t} \equiv c_{,t} + (\mathbf{u}\cdot\nabla)c = 0, \qquad 1.$$

using a comma-subscript notation to denote a derivative (here with respect to time, t). c is passive if its distribution has no influence on $\mathbf{u}$. Operating on this by $[\nabla c \cdot \nabla]$ yields the Lagrangian frontogenetic tendency equation for c:

$$\frac{1}{2}\frac{\mathrm{D}}{\mathrm{D}t}[c_{,k}c_{,k}] = -u^{\ell}_{,k}c_{,k}c_{,\ell} \equiv \mathcal{T}^c. \qquad 2.$$

Here, k and ℓ are spatial coordinate indices, and summation occurs over repeated indices. This implies that, following the flow, the squared gradient of c will increase at a rate $2\mathcal{T}^c$, which is proportional to the velocity gradient (i.e., shear) tensor, $u^{\ell}_{,k}$. $\mathcal{T}^c > 0$ indicates frontogenesis, and $\mathcal{T}^c < 0$ indicates frontolysis. The advantage of a Lagrangian-frame diagnostic is that it separates gradient sharpening from movement.

In one dimension (1D), $\mathcal{T}^c$ is equal to $-u^x_{,x}c^2_{,x}$, and frontogenesis occurs where the divergence, $\delta = u^x_{,x}$, is negative, i.e., in a convergence zone.

In two dimensions (2D), with $i, j = (x, y)$ the horizontal coordinates, the shear tensor $u^j_{,i}$ can be linearly decomposed in terms of horizontal divergence $\delta = u^x_{,x} + u^y_{,y}$, vertical vorticity $\zeta = u^y_{,x} - u^x_{,y}$, and two components of horizontal strain rate, normal and shear (**Figure 2**). For the present

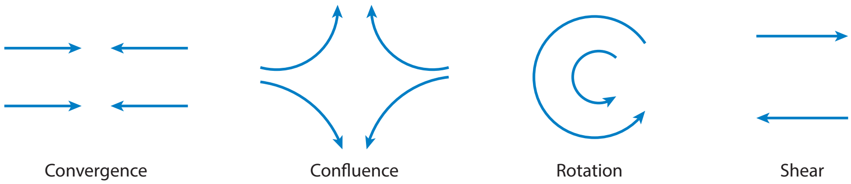

Figure 2

Two-dimensional flow types analyzed in Section 2 for their frontogenetic tendencies for the advection of a passive tracer $c(x, y)$.

purposes, with a focus on $c_{,x}$, the strain rate pair is expressed in terms of normal strain, $2\alpha = u^y_y - u^x_{,x}$, and shear strain, $2Sh = u^x_y + u^y_{,x}$.

For divergence only (e.g., $u^x = \delta x$ and $u^y = 0$), the frontogenetic tendency is $\mathcal{T}^c = -\delta c^2_{,x}$, the same as in 1D. This is positive definite if $\delta < 0$ (i.e., horizontal convergence), and then there will be an exponential growth of the gradient magnitude in time, $|\nabla c|^2 \sim e^{-2\delta t}$.

For vorticity only, this simplest case is solid-body rotation expressed in polar coordinates, $u^r = 0$ and $u^\theta = \Gamma r$, and it has $\mathcal{T}^c = 0$; i.e., the pattern in c simply rotates at a rate Γ. If u^θ is a general function of r, then $\mathcal{T}^c$ is equal to $-[u^\theta/r]_{,r} c_{,r} c_{,\theta}$. For general $c(r, \theta)$, this is not sign definite even if the velocity gradient factor is; i.e., some regions will be frontogenetic, and some frontolytic. Usually there will be gradient growth in some places, but at a weaker time dependency than with convergence; i.e., $|\nabla c| \propto |\partial_r[u^\theta(r)/r]|t$ as $t \to \infty$.

For deformation only—e.g., normal strain with $u^x = -\alpha x$, $u^y = +\alpha y$, and $\alpha > 0$ (a confluent flow in toward and out along the y axis)—$|c_{,x}|$ will grow while $|c_{,y}|$ will decrease, and $|\nabla c|^2$ is proportional to $e^{2\alpha t}$, again a positive-definite frontogenesis with an exponential rate of sharpening. Alternatively, for the case of pure shear strain (e.g., $u^x = Shy$ and $u^y = Shx$), the gradients will evolve by rotating in (x, y) until they are favorably aligned with $\mathbf{u}$, after which deformation frontogenesis will ensue.

For shear only (e.g., $u^x = Sy$ and $u^y = 0$), $\mathcal{T}^c$ equals $-Sc_{,x}c_{,y}$, which again is nonsystematic as frontogenesis and has at most a linear rate of gradient growth (as with vorticity), $|\nabla c| \propto |S|t$ at late time.

In all of these kinematic paradigms, $c(x, y, t)$ will evolve, and the pattern and magnitude of $\mathcal{T}^c$ will change, even more so if $\mathbf{u}$ has a complex spatial structure and is evolving. Nevertheless, the 2D velocity fields of convergence and deformation will induce systematic frontogenesis with an exponential growth in gradient magnitude and a corresponding shrinkage in the width ℓ for the high-gradient zones in a Lagrangian reference frame following the flow.

Finally, in nature's three dimensions (3D), Equations 1 and 2 are recast to focus on the horizontal gradient that is the usual identifier for oceanic fronts, i.e.,

$$\frac{1}{2}\frac{\mathrm{D}}{\mathrm{D}t}[c_{,i}c_{,i}] = -u^j_{,i}c_{,i}c_{,j} - w_{,i}c_{,i}c_{,z} \equiv \mathcal{T}^c, \qquad 3.$$

with the velocity split into its horizontal and vertical components, $\mathbf{u} = (u^i, w)$. z is the upward coordinate parallel to gravity, and the indices i and j are henceforth restricted to (x, y). Near the oceanic surface at $z \approx 0$, the vertical velocity w is small compared with its interior values for non-gravity-wave currents, and $w_{,z}$ is large. This is equally true near the bottom boundary, where a vanishing normal velocity on a weakly sloping bottom implies a small w and sometimes large $w_{,z}$. Underneath a surface convergence with $\delta < 0$, w is negative (downwelling), $w_{,z} > 0$; the near-bottom analog is an upwelling w but still with $w_{,z} > 0$. This surface configuration is conducive to frontogenesis (Lapeyre et al. 2006), and it is usually the horizontal velocity shear terms in Equation 3 that are frontogenetic. Because $c_{,z}$ is often weak in the mixed layer near the surface, the w gradient term in Equation 3 is usually weaker and at least partly frontolytic (i.e., weakening the horizontal gradient). Furthermore, with $w_{,z} > 0$ locally, the Lagrangian vorticity tendency equation partly manifests cyclonic vertical vorticity ($\zeta/f > 0$) generation in the front where there is horizontal convergence—i.e., $\mathrm{D}\zeta/\mathrm{D}t \sim f w_{,z} > 0$ (where f is the Coriolis frequency). These aspects are further discussed in Section 3.

3. DYNAMICS

The dynamical view of fronts and frontogenesis connects the circulation to the buoyancy, $b = -g\rho/\rho_0$ (where g is gravitational acceleration, and ρ_0 is a reference density). For a simple equation of state, the Lagrangian frontogenetic tendency equation for b is isomorphic to Equation 3 with $c = b$:

$$\frac{1}{2}\frac{\mathrm{D}}{\mathrm{D}t}[b_{,i}b_{,i}] = -u^j_{,i}b_{,i}b_{,j} - w_{,i}b_{,i}b_{,z} \equiv \mathcal{T}^b. \qquad 4.$$

Its counterpart for the horizontal velocity gradient magnitude is

$$\begin{aligned}\frac{1}{2}\frac{\mathrm{D}}{\mathrm{D}t}[u^i_{,j}u^i_{,j}] &= -u^j_{,i}u^k_{,i}u^j_{,k} - w_{,i}u^j_{,i}u^j_{,j} - u^j_{,i}\phi_{,ij} - u^j_{,i}F^j_{,i}\\ \equiv \mathcal{T}^u &= \qquad\quad \mathcal{T}^u_{ad} \qquad\quad + \quad \mathcal{T}^u_\phi + \mathcal{T}^u_F.\end{aligned} \qquad 5.$$

Here, $\phi = p/\rho_0$ is the normalized pressure, and F^i is the horizontal nonconservative force vector (e.g., small-scale momentum mixing). The Coriolis force in the traditional f-plane approximation does not contribute to $\mathcal{T}^u$. Also, notice that the gravitational force does not appear explicitly in Equation 5, even though it is intimately involved in frontogenesis. From the perspective that ϕ is often determined to enforce incompressibility in high-Reynolds-number flows (i.e., the Laplacian of ϕ balances the divergence of momentum advection and $\mathbf{F}$), it sometimes makes sense to combine $\mathcal{T}^u_{ad} + \mathcal{T}^u_\phi$. In many situations, the gradients of b and $\mathbf{u}$ (and neighboring c) sharpen together, and Equations 4 and 5 provide a frontogenetic diagnostic framework.

3.1. Quasi-Geostrophic Frontogenesis

Historically, much of the meteorological interest in weather fronts has been in the context of extratropical cyclones, with their associated warm and cold frontal lines. Quasi-geostrophic theory provides an entry into this behavior (Hoskins 1982, Davies 1999), and, as is often the case in geophysical fluid dynamics, it allows a more extensive and succinct analysis than do more general models. Even though it is formally valid only for weak fronts, its solutions provide useful paradigms for stronger fronts (Section 3.4).

Quasi-geostrophic theory starts with a decomposition of the horizontal velocity into geostrophic and ageostrophic components,

$$u^i = u^i_g + u^i_a, \qquad u^i_g = \frac{1}{f}\epsilon_{izk}\phi_{,k}. \qquad 6.$$

Here, ϵ is the Levi–Civita tensor, which represents a vector cross-product: $\epsilon = 0$ unless the indices are some permutation of xyz, $\epsilon = 1$ if an even permutation, and $\epsilon = -1$ if an odd one. The usual expression of the theory is geostrophic balance in the horizontal-momentum equations, $f\epsilon_{izj}u^j_g = -\phi_{,i}$; hydrostatic balance in the vertical-momentum equation, $\phi_{,z} = b$; and the elimination of w among the vertical-vorticity, buoyancy-conservation, and continuity equations to yield a prognostic evolution equation for the conservation of quasi-geostrophic potential vorticity, $q = f + \epsilon_{zij}u^j_{g,i} + fb/N^2$, where $N(z)$ is the buoyancy frequency profile associated with the background stratification, $N^2(z) = \overline{b}_{,z}$, and b is the 3D deviation from $\overline{b}$. The formal justification of this theory is as an asymptotic approximation in small Rossby number, $Ro = V/fL$, where the right-side quantities are characteristic scales for horizontal velocity, Coriolis frequency, and horizontal length (Pedlosky 1987).

From the perspective of frontogenesis, a more cogent expression of quasi-geostrophic theory is to write the conservative ($F^i = 0$) momentum, buoyancy, and continuity equations as follows:

$$D_g u_g = f v_a, \quad D_g v_g = -f u_a, \phi_{,z} = b, \quad D_g b = -N^2 w, u^i_{a,i} + w_{,z} = 0. \qquad 7.$$

Here, geostrophic balance has been subtracted from the horizontal-momentum equations, u^i equals (u, v), and $D_g[\cdot] = [\cdot]_{,t} + u^j_g[\cdot]_{,j}$ is the geostrophic advective time derivative. This formulation makes explicit the role of the 3D ageostrophic currents, (u^i_a, w), as diagnostic balances with the time tendencies in u^i_g and b. Together with Equation 6, this is a complete specification of quasi-geostrophic dynamics. It is well ordered in Ro, i.e., all terms here are of the same order; this is not true for the primitive momentum equations.

By taking the horizontal derivative of the b equation in Equation 7, the buoyancy gradient equation is

$$D_g b_{,i} = Q^i - N^2 w_{,i}, \qquad Q^i \equiv -u^j_{,gi} b_{,j}, \qquad 8.$$

where Q^i is called the Q-vector (Hoskins & Draghici 1977). From this, it follows that $\mathcal{T}^b_g = u^i Q^i - w_{,i} b_{,i} N^2$. Q^i thus partly controls the Lagrangian evolution of the buoyancy gradient, and it is the primary agent of deformation frontogenesis.

An analogous result for quasi-geostrophic velocity frontogenesis is derived from taking the gradient of the horizontal-momentum equations shown in Equation 7:

$$\frac{1}{2} D_g[u^i_{g,j} u^i_{g,j}] = \mathcal{T}^u_g \equiv f \epsilon_{z\ell m} u^\ell_{g,j} u^m_{a,j}. \qquad 9.$$

Note that the geostrophic part of $\mathcal{T}^u_{ad}$ is zero (a general result because of $u^j_{g,j} = 0$), the geostrophic contributions from the pressure gradient and Coriolis force are zero, and the ageostrophic Coriolis force emerges as the only conservative term in $\mathcal{T}^u_g$.

Deformation and convergence are the two kinematic types of systematic frontogenesis (Section 2), and only the former can occur with the quasi-geostrophic approximation because the geostrophic current is nondivergent, $u^i_{g,i} = 0$; hence, the convergence is only ageostrophic and is neglected in Equation 6. Therefore, the focus here is on deformation frontogenesis.

By manipulating Equation 7 to eliminate the time-derivative terms, one obtains the so-called omega equation for the vertical velocity w:

$$f^2 w_{,zz} + N^2 w_{,ii} = 2Q^i_{,i}. \qquad 10.$$

The left-side operator is elliptic when $N^2 > 0$ (i.e., stable stratification). The second left-side term has a relative magnitude compared with the first one of the Burger number, $Bu = (Nh/f\ell)^2$. In a surface mixed layer with weak stratification, Bu is much less than 1, and the first term is dominant. The omega equation is a popular diagnostic for vertical motion in synoptic meteorology, and it is also useful in diagnosing the secondary circulation in frontogenesis (within a small-Ro approximation).

The energy source for frontogenesis is the potential energy associated with the horizontal buoyancy gradient $b_{,i}$. It is expressed as the difference between the potential energy of the actual buoyancy field and the potential energy of a stratified reference state defined by adiabatically flattening all the buoyancy surfaces, called the available potential energy. Its local formula is

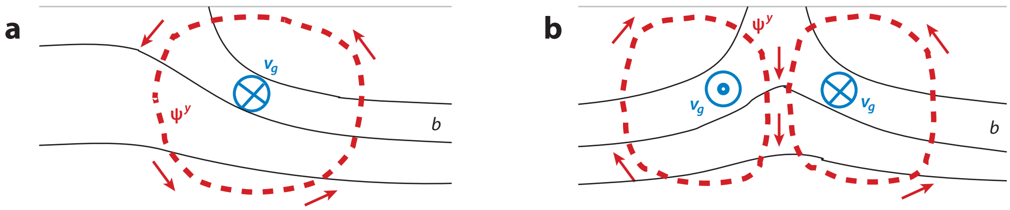

Figure 3

The buoyancy (b, *black*), geostrophic along-front current (v_g, *blue*), and cross-front overturning streamfunction (Ψ^y) in the (x, z) plane for (*a*) a front with its dense side on the left and (*b*) a dense filament at the oceanic surface. A centered dot indicates the head of a vector (into the page in the $+y$ direction), and a centered cross indicates a tail. These flow configurations are valid for the presence of both an ambient deformation flow and vertical-momentum mixing, i.e., quasi-geostrophic deformation and turbulent thermal wind convergent frontogenesis (Sections 3.1 and 3.2).

$APE = b^2/(2N^2)$ in the quasi-geostrophic model. From Equation 6, its balance equation is derived as

$$D_g[APE] = -wb, \qquad 11.$$

where the right side represents energy conversion from potential to kinetic energy when wb is positive in a volume integral. (This potential energy conversion term is the same for more general fluid dynamics.) Notice that it is associated entirely with the ageostrophic secondary circulation.

For a 2D surface front, $b(x, z)$, with an externally imposed barotropic deformation flow with strain rate α and a surface-intensified, geostrophic along-front flow (i.e., $u_g = -\alpha x$, $v_g = \alpha y + \int^z b_{,x}/f \mathrm{d}z'$), frontogenesis occurs. When $\alpha = 0$, this configuration is a quiescent front with the geostrophic jet as its only flow and with no further time development. With $\alpha \neq 0$, Q^x equals $\alpha b_{,x}$ and Q^y equals 0. Thus, $\mathcal{T}_g^b = \alpha(b_{,x})^2$ is greater than 0 when α is greater than 0 (i.e., when the front and the deformation flow are aligned favorably for frontogenesis); this relation implies an exponential rate of temporal growth in the buoyancy gradient magnitude (Section 2).

Consider in particular the $b(x, z)$ frontal configuration sketched in **Figure 3*a***, where the buoyancy anomaly $b_{,x}$, and hence the frontal component of v_g, vanishes with depth. The associated pattern in v_g is an along-front jet. In the omega equation (Equation 10), the right-side term is $u_{,x}Q^x = 2\alpha b_{,xx}$; this is negative on the light side of the front and positive on the dense side. Because the left-side omega operator is elliptic, its inversion yields a w that has upwelling on the light side and downwelling on the dense side; i.e., the product wb tends to be positive, which implies an upward (restratifying) buoyancy flux (Lapeyre et al. 2006) and a positive integrated conversion of potential to kinetic energy in Equation 11. Thus, deformation frontogenesis acts to increase the vertical stratification and increases its kinetic energy at the expense of the horizontal density gradients.

The system shown in Equation 7 implies $v_a = \alpha^2 x$ in this case, which is doubly small compared with the frontal $v_g(x, z)$ if $(\alpha/f)^2 \ll 1$; by contrast, u_a is only smaller by the linear scaling factor, α/f. Thus, the w pattern implies a closed recirculation in the frontal plane, as also sketched in **Figure 3*a***. A more explicit characterization of the ageostrophic secondary circulation comes from the Sawyer–Eliassen equation for the nondivergent, ageostrophic streamfunction $\Psi^y(x, z)$, with $u_a = \Psi^y_{,z}$ and $w = -\Psi^y_{,x}$, also derived from Equation 7 in this case, again by eliminating time-derivative terms in favor of Ψ^y derivatives:

$$f^2 \Psi^y_{,zz} + N^2 \Psi^y_{,xx} = -2Q^x = -2\alpha b_{,x} \qquad 12.$$

(Hoskins & Draghici 1977). This is recognizable as a first integral in x of Equation 10. It yields a positive monopole pattern for Ψ^y in the center of the front, consistent with the secondary circulation sketched in **Figure 3*a***. In Equation 9, $\mathcal{T}_g^u$ is equal to $-fv_{g,x}u_{a,x}$, and with v_g a positive jet and u_a a negative (westward) flow near the surface (**Figure 3*a***), this is a positive quantity (frontogenetic) in the upper part of the front and more weakly negative (frontolytic) in the lower part. Furthermore, even though they are missing in the quasi-geostrophic approximation, from Equations 4 and 5 the contributions in $\mathcal{T}^b$ of $-u_{a,x}(b_{,x})^2$ and in $\mathcal{T}_{ad}^u$ of $-(u_{a,x})^3$ are to be expected in the general fluid-dynamical model; these quantities are positive where there is ageostrophic surface convergence, $-u_{a,x} > 0$, on the dense side of the front, which foreshadows the superexponential rate of frontogenesis discussed in Section 3.4. As the magnitude of $b_{,x}$ grows in time, $v_{g,z}$ grows along with it; an interpretation of the role of u_a is that it acts to maintain this geostrophic balance during frontogenesis (Hoskins & Draghici 1977).

Also shown in **Figure 3*b*** is an analogous $b(x, z)$ and $\mathbf{u}$ configuration for a dense surface filament; in a sense, a dense filament is simply a two-sided front with dense water in the middle. Dense filaments are commonly seen on the oceanic surface in measurements and models (and probably in the lower atmosphere as well, although not so famously as fronts); see Section 4.3. A filament has a double jet structure for the surface-intensified $v_g(x, z)$. In the same barotropic deformation flow as in the preceding paragraphs, analogous analyses can be made. The results are a two-celled (dipole) secondary circulation with downwelling in the filament center, again a generally positive wb, and again positive frontogenetic tendencies $\mathcal{T}_b^b$ and $\mathcal{T}_g^u$ on the flanks of the surface buoyancy minimum, as well as the implication of a higher-order $\mathcal{T}_{ad}^u > 0$ at these places. In the geostrophic approximation, the frontogenetic rate, $\mathcal{T}^b = \alpha(b_{,x})^2$, is equally strong for either a warm or dense filament as it is for a front with the same $b_{,x}$ strength. However, because of the implied ageostrophic convergence contributions to $\mathcal{T}^b$ and $\mathcal{T}_{ad}^u$, a dense filament is expected to be more strongly frontogenetic than a front, while a light filament, because of its reverse secondary circulation, is less frontogenetic (McWilliams et al. 2009a); this explains the relative rareness of light surface filaments on the oceanic surface.

A scaling analysis for quasi-geostrophic frontogenesis is based on two types of Rossby numbers for the frontal and deformation flows, respectively:

$$Ro_f = \frac{V}{f\ell}, \qquad Ro_d = \frac{\alpha}{f}, \tag{13}$$

where V is a geostrophic velocity scale $\sim h(\Delta b)/f\ell$. In an oceanic mesoscale-eddy field, one expects α to represent the eddy strain rate $\sim V/\ell$, so typically $Ro_f \sim Ro_d$ at the initiation of frontogenesis. From the relations above, relevant quantities have the following scaling estimates:

$$u_a \sim Ro_d V, \quad w \sim Ro_d \frac{Vh}{\ell}, \quad wb \sim \alpha V^2, \quad \mathcal{T}_g^b \sim \alpha\left(\frac{Vf}{h}\right)^2, \quad \mathcal{T}_g^u \sim \alpha\left(\frac{V}{\ell}\right)^2, \tag{14}$$

and the implied ageostrophic convergence frontogenetic tendencies at higher order are

$$\mathcal{T}_a^b \sim Ro_f\, \mathcal{T}_g^b, \quad \mathcal{T}_{ad}^u \sim Ro_d^2\, Ro_f\, \mathcal{T}_g^u. \tag{15}$$

Because frontogenesis shrinks the width ℓ, Ro_f is expected to increase with time, while Ro_d does not if the frontal environment does not change. Thus, the first quantity in Equation 15 is smaller only by the increasing factor Ro_f, while the second is much smaller by the factor $Ro_d^2 Ro_f$.

It should also be remarked that quasi-geostrophic frontogenesis can additionally occur in background flows with vertical vorticity or horizontal shear, albeit less systematically than with deformation (Section 2). In particular, another popular conception for meteorological fronts is an initially 2D $b(x, z)$ field in the presence of a background shear $u(y)$ (Davies 1999); its evolution quickly becomes fully 3D in b and u_g^i.

3.2. Turbulent Thermal Wind

Another frontogenetic process is associated with the vertical-momentum mixing that is almost always present in the surface boundary layer due to the turbulence generated by wind stress or convection (Gula et al. 2014, McWilliams et al. 2015). Its simplest model is

$$f\epsilon_{izk}u^k = -\phi_{,i} + [\nu u^i, z]_{,z}, \quad \phi_{,z} = b, \quad u^i_{,i} + w_{,z} = 0, \qquad 16.$$

i.e., a linear horizontal force balance among Coriolis, pressure-gradient, and vertical-momentum diffusion with an eddy viscosity $\nu(\mathbf{x}) \geq 0$ parameterization for the turbulent vertical Reynolds-stress divergence,

$$-[\overline{w'u^{i'}}]_{,z} \longrightarrow \nu(z)\overline{u}^i_{,z}. \qquad 17.$$

It is a combination of the familiar Ekman-layer and geostrophic models, and is thus called turbulent thermal wind (TTW). There is no a priori assumption of small *Ro* here; nevertheless, if a geostrophic–ageostrophic decomposition (Equation 6) is made, and it is assumed that $\nu(\mathbf{x})$ is nonzero only near the surface, then Equation 16 can be rewritten as a 1D elliptic ordinary differential equation system for the ageostrophic flow $(u^i_a, w)(z)$ in the presence of b, ν, and the surface wind stress $\boldsymbol{\tau}^i_w$:

$$f\epsilon_{izk}u^k_a - [\nu u^i_{,z}]_{,z} = [\nu u^i_{g,z}]_{,z}, \qquad w = \int_z^0 u^i_{a,i}\mathrm{d}z', \qquad 18.$$

with boundary conditions $w = 0$ and $\nu u^i_{a,z} = -\nu u^i_{g,z} + \boldsymbol{\tau}^i_w/\rho_0$ at the mean sea level, $z = 0$, and $u^i_a \to 0$ in the deep interior as $z \to -\infty$. The problem for $u^i_a(z)$ is readily solved at each x^i and t, and then a horizontal derivative can be taken to evaluate $w(\mathbf{x})$.

As in Section 3.1, consider a 2D front or filament with $b(x, z)$, and hence $v_g = \int^z b_x/f\mathrm{d}z'$. If $\nu = 0$, the front is quiescent. With nonzero ν, the resulting TTW $u^i_a(z)$ profiles are sketched in **Figure 4**. For $f > 0$, the surface ageostrophic velocities are leftward and rearward of the geostrophic current, and they spiral to the right with depth, as in an Ekman layer. Without wind stress, there is no ageostrophic horizontal transport, $\int_{-\infty}^0 u^i_a\mathrm{d}z' = 0$, so $w(z)$ is confined within the boundary layer.

When these TTW vertical profiles are composited across x, the remarkable result is that the secondary circulation, restratification flux, potential energy conversion, and $\mathcal{T}^b$ and $\mathcal{T}^u$ advective

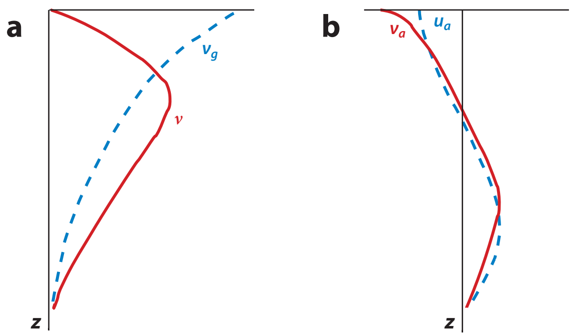

Figure 4

The shapes of (*a*) a northward geostrophic along-front velocity $v_g(z)$ and vertical eddy viscosity $\nu(z)$ (*dashed* and *solid lines*, respectively) and (*b*) the turbulent thermal wind ageostrophic velocities, $u_a(z)$ and $v_a(z)$ (*dashed* and *solid lines*, respectively). The convex shape of $\nu(z)$ is typical for a turbulent boundary layer; however, the profiles of $u^i_a(z)$ are qualitatively similar even with a constant ν. For simplicity, τ_w is 0 here; otherwise, the $u^i_a(z)$ profiles would additionally exhibit an Ekman current spiral (McWilliams 2017).

frontogenetic tendencies all have the same signs and qualitative shapes as for quasi-geostrophic deformation frontogenesis of density fronts and filaments (**Figure 3**). In the present case, however, the frontogenesis is due entirely to the surface ageostrophic convergence, $-u_{a,x} < 0$, that occurs near the surface either on the dense side of a front or the center of a dense filament. The mathematical prescriptions for w and Ψ^y are implicit in Equation 18, unlike their explicit forms in Equations 10 and 12.

Because of the structural similarity in b and $\mathbf{u}$, as well as their frontogenetic behavior and energy source in common, it is not simple to distinguish between deformation and TTW processes in measurements, at least not without also inquiring into the associated strain rate α and eddy viscosity ν fields. Both mesoscale-eddy strain and boundary-layer turbulence are ubiquitous in the surface ocean, and both are highly variable in their magnitudes. Deformation frontogenesis by normal strain depends on a favorable orientation between $b_{,i}$ and the axis of confluence, although shear strain can rotate the buoyancy gradient toward this alignment (Section 2); by contrast, TTW frontogenesis acts for any orientation of $b_{,i}$.

For a scaling analysis of TTW frontogenesis, one uses the same frontal velocity scale of $V \sim h(\Delta b)/fh$ (Section 7). The ageostrophic current estimates are

$$u_a^i \sim EkV, \qquad w \sim Ek\left(\frac{Vh}{\ell}\right), \qquad wb \sim Ek\, fV^2, \tag{19.}$$

where $Ek = \nu/fh^2$ is the turbulent Ekman number. Ek is often not small; e.g., for a brisk wind in the subtropics, with $\tau_w \approx 0.1$ N m^2, $\nu \approx 0.1$ m^2 s^{-1}, $f \approx 10^{-4}$ s^{-1}, and $h \approx 30$ m, Ek is approximately 1. Thus, the TTW secondary circulation is not necessarily weak compared with the along-front current. Scaling estimates for the TTW frontogenetic tendencies are

$$\mathcal{T}^b \sim Ek\left(\frac{V}{\ell}\right)\left(\frac{Vf}{h}\right)^2, \qquad \mathcal{T}^u \sim Ek(1+Ek^2)\left(\frac{V}{\ell}\right)^3 \tag{20.}$$

(McWilliams 2017). The $1 + Ek^2$ factor indicates that both $v_{g,x}$ and $u_{a,x}$ terms contribute to $\mathcal{T}^u$ here.

A comparison of u_a^i for TTW with a wind-driven Ekman current has the scaling ratio $\sim \nu V/hu_*^2$, where $u_* = \sqrt{|\tau_w|/\rho_0}$ is the so-called friction velocity. Because $\nu \sim u_* h$ in a turbulent Ekman layer, this ratio is V/u_*, which is often large. An analogous comparison for u_a with deformation in Equation 14 has the ratio $\sim EkV/\alpha\ell = Ek\, Ro_f/Ro_d$. As Ro_f increases through frontogenesis, this ratio will increase. The same ratio holds for the comparison of $\mathcal{T}^b$ estimates. The scaling ratio between TTW $\mathcal{T}^u$ and $\mathcal{T}_g^u$ in Equation 14 is $\sim Ek\,(1 + Ek^2)\, Ro_f/Ro_d$; again, it often is not small and increases with time. The ratio of potential-to-kinetic-energy conversion estimates in Equations 19 and 14 is $\sim Ek/Ro_d$.

Wind stress is not the only cause of vertical-momentum mixing. In the case of a convective surface buoyancy flux $\overline{w'b'}(0) \equiv \mathcal{B} > 0$, the turbulent wind-stress velocity scale $V \sim u_*$ is replaced by the convective scale $V \sim w_* = (\mathcal{B}h)^{1/3}$, both with $\nu \sim Vh$. If the momentum mixing is due to vertical shear instability with Richardson number $Ri = N^2/(\overline{u}^i_{,z})^2 \lesssim 1$, then this can locally be the source for a turbulent $\nu(z)$.

For the several reasons given above, the expectation is that TTW frontogenesis will be at least as important a process as deformation frontogenesis in the oceanic surface layer, especially at the submesoscale, where Ro_f is often not small, while mesoscale Ro_d usually is small (Section 4.3). While at first thought it might seem odd that the presence of vertical mixing leads to frontogenesis, even in the absence of large-scale strain of the geostrophic shear flow, it does occur because the associated secondary circulation has a surface convergence (Section 2).

3.3. Gravitational Steepening

The ocean is full of gravity waves, in association both with the air–sea interface and with the internal density stratification N. Linear gravity waves propagate, disperse, refract, reflect, diffract, and scatter. Nonlinear gravity currents steepen on their forward-propagating face, and given time and distance, this steepening will become a frontal face—often called a bore—that might subsequently become arrested in width (e.g., through dispersion, as in a shape-preserving soliton wave), become unstable and fragment into turbulence, or break and then spill or overturn (Benjamin 1966, 1968; Long 1972; Simpson & Linden 1989). The nonlinear instability and breaking processes are highly dissipative and effect strong local material mixing across the stratification. Regarding the terminology, a distinction can be made between gravity oscillations, where advective steepening occurs at certain phase locations, and gravity currents, where the steepening occurs primarily at the leading edge of a propagating layer of anomalous density (light if above, and dense if below). These phenomena are also common in the atmosphere, and they have an extensive literature (Simpson 1997).

A simple model for gravity frontal steepening is the conservative, hydrostatic, nonrotating, shallow-water equations in 1D (x):

$$u_{,t} + uu_{,x} = -g\eta_{,x}, \qquad \eta_{,t} + [hu]_{,x} = 0, \tag{21}$$

where $u(x, t)$ is the velocity, H is the mean layer depth, $\eta(x, t)$ is the fluctuation in the height of its gravitational interface, $h = H + \eta$ is the total layer depth, and g is the gravitational acceleration [note that often $g' = g(\Delta\rho)/\rho_0$ for an internal interface with density jump $\Delta\rho$]. For dimensional comparability with stratified flows, the interface height is rescaled as a buoyancy variable, defined as $b = g\eta/H$.

The system shown in Equation 21 has nondispersive linear wave solutions with

$$\eta = a\mathcal{G}(x - ct), \qquad u = u_0\mathcal{G}(x - ct). \tag{22}$$

Here, a is the wave height, $u_0 = ga/c$ is the velocity amplitude, c is the phase speed, c^2 equals gH, and $\mathcal{G}(s)$ with argument $s = x - ct$ is the wave shape that is invariant during propagation. (A uniform environment with respect to H and horizontal boundaries is assumed.)

The corresponding Lagrangian frontogenetic tendency equations are

$$\begin{aligned}
\frac{1}{2}\frac{\mathrm{D}}{\mathrm{D}t}[\eta_{,x}\eta_{,x}] &= \mathcal{T}^\eta \equiv -2u_{,x}(\eta_{,x})^2 - h\eta_{,x}u_{,xx} \\
&= -2u_0a^2\,(\mathcal{G}_{,s})^3 - \frac{hu_0a}{2}\,[(\mathcal{G}_{,s})^2]_{,s}, \\
\frac{1}{2}\frac{\mathrm{D}}{\mathrm{D}t}[u_{,x}u_{,x}] &= \mathcal{T}^\eta \equiv -u_{,x}^3 - gu_{,x}\eta_{,xx} \\
&= -u_0^3(\mathcal{G}_{,s})^3 - \frac{gu_0a}{2}[(\mathcal{G}_{,s})^2]_{,s}.
\end{aligned} \tag{23}$$

Here, $\mathrm{D}(\cdot)/\mathrm{D}t$ is equal to $(\cdot)_{,t} + u(\cdot)_{,x}$. Thus, both $\mathcal{T}^\eta$ and $\mathcal{T}^u$ have analogous component tendencies, albeit with different amplitude prefactors. These tendencies are functions of s, and thus they are expressed in the reference frame of the propagating disturbance, while the implicit advective tendencies on the left sides refer to the parcel velocity frame, which generally will lag the propagation frame until a gravity bore develops. Nevertheless, the right-side tendencies have quite simple general interpretations for how the shape will evolve.

Consider a simple sloping step-function interface (e.g., a nondimensional $\mathcal{G}(s) = \pm\tanh[s/\ell]$). With the convention that $a > 0$, the minus sign is taken for $\mathcal{G}$, and $c > 0$ (i.e., $u_0 > 0$), the slope faces forward in the direction of propagation and vice versa for a backward slope. In Equation 23 for a forward slope, the velocity is convergent, $-u_{,x} > 0$, and the first left-side terms are sign definite, with $-(\mathcal{G}_{,s})^3 > 0$, i.e., frontogenetic. The second left-side terms are sign alternating, and their net effect in an integral over s is zero, even though locally they can act to reshape the wave face. Thus, a forward face will steepen overall. By contrast, a backward face will have a divergent velocity and broaden overall. (The $c < 0$ case is easily worked out, with different signs of the u_0 and a prefactors in Equation 23, but the conclusion is the same that forward and backward faces steepen and broaden, respectively.) In the shallow-water model shown in Equation 21, and more generally, frontogenesis can be accelerated by shoaling topography or, in the case of a dense bottom anomaly, by downhill propagation.

A scaling analysis with $b = g\eta/H$ yields $u \sim V = ga/c = (\Delta b)\sqrt{H/g}$, with again $w \sim VH/\ell$ based on $w = \mathrm{D}\eta/\mathrm{D}t$. The potential energy conversion wb is proportional to $[\mathcal{G}^2]_{,s}$ and thus has zero integral in s. However, as noted in Section 4.4, a gravity wave exhibits reversible recycling between kinetic and potential energies during different phases, so local values of wb are more meaningful for frontogenesis than are integrated ones. The scaling estimates for the frontogenetic tendencies associated with the first right-side terms in Equation 23 are

$$\mathcal{T}^b \sim \frac{g}{H}\left(\frac{V}{\ell}\right)^3, \qquad \mathcal{T}^b \sim \left(\frac{V}{\ell}\right)^3. \qquad 24.$$

These can be compared with Equations 14, 15, and 20 to see the roles of the different parameters.

Beyond this analysis, which projects the frontogenetic tendency of the linear shallow-water solution, it is well known that highly nonlinear gravity fronts frequently occur in nature. They involve steepening the forward face while developing small-scale turbulence there. The most useful oceanic paradigm is as a gravity current (e.g., from river inflows at the surface and shoaling internal tides and dense water overflows at the bottom), whose head undergoes frontogenesis and whose body often involves a sustained vertical shear instability (i.e., Kelvin–Helmholtz) at the interface between the different densities above and below. Within hours, the gravity current evolution will become influenced by Earth's rotation, which acts to slow the propagation speed and turn the current along-front (Ungarish & Huppert 1998). Nevertheless, the frontogenesis for gravity fronts is unambiguously caused by horizontal convergence.

3.4. Strong Three-Dimensional Frontogenesis

The preceding subsections present simple, quasi-linear, 1D and 2D theoretical models that demonstrate the initiation of frontogenesis for the three different types of processes. Now consider a more general frontal dynamics that develops 3D structure and becomes significantly nonlinear with ageostrophic advection with $Ro \gtrsim 1$ as frontogenesis proceeds.

With a few exceptions, this requires going beyond the simpler theories that have their validity in the regimes of relatively weak fronts (Sections 3.1–3.3), by moving to a computational-simulation methodology. To the extent that frontogenesis involves significant energy transfer across widely different horizontal scales, this methodology usually requires large computational grids and/or grid nesting with high resolution in the frontal zone. This computational approach has blossomed in recent years. In many circulation-model simulations of strong frontogenesis, the necessary model regularization near the grid size (e.g., diffusion, with $\ell \sim \sqrt{\kappa/|\nabla \mathbf{u}|}$) causes a frontal arrest before a frontal instability manifests, but turbulence-resolving Large Eddy Simulations can overcome this limitation (Section 3.5).

It is often said (e.g., Section 1), with an intimation of high drama, that some frontogenesis models predict a finite-time singularity. The important implication of this is that frontogenesis is a very efficient transformation process of the flow structure toward smaller scales, and hence to energy dissipation. The same can also be said of Kolmogorov's conception of the turbulent energy cascade, where from smooth initial conditions the onset of dissipation will occur in a finite time, no matter how large the Reynolds number is. [This is a corollary to the finite-time predictability horizon for 3D turbulence no matter how good the initial-condition observing system is (Lorenz 1969).] What is distinctive about frontogenesis is the way that its ℓ collapse occurs within a single type of coherent structure, rather than as the incoherent transfers usually associated with generic turbulence—at least until 3D frontal instabilities intervene (Section 3.5).

The theory of strong frontogenesis has been enormously influenced by the semigeostrophic model (Hoskins & Bretherton 1972; Hoskins 1982, 2003). Its essential assumption is a momentum balance where $\mathrm{D}u^i/\mathrm{D}t$ is approximated by $\mathrm{D}u^i_g/\mathrm{D}t$. In the particular circumstances of a 2D $b(x,z)$ front and an assumption of uniform potential vorticity (as defined in this approximation), it yields an analytic solution that proceeds to a finite-time singularity in $b_{,j}$. It assumes a small ratio between the cross- and along-front velocity magnitudes $|u|/|v|$ (and hence also between divergence and vorticity, $|\delta|/|\zeta| \ll 1$), even as Ro_f becomes large; nevertheless, its late-time frontogenetic rate is controlled by the ageostrophic surface convergence, $-\delta \approx -u_{a,x}$, rather than by the background deformation rate, α (cf. Section 3.1).

Semigeostrophic theory has a large audience in the context of the emergence of weather fronts in the life cycle of baroclinic waves in the jet stream that grow into extratropical cyclones, i.e., a 3D phenomenon. While this is widely seen as a useful paradigm for strong frontogenesis, several cautions can be stated: (*a*) Semigeostrophy in general is not a consistent asymptotic improvement over quasi-geostrophy in Ro (McWilliams & Gent 1980); (*b*) more particularly, even for horizontally anisotropic flows like fronts, semigeostrophy loses formal accuracy when there is even moderate frontal curvature (Gent et al. 1994); and (*c*) in more general fluid-dynamical simulations of the above-mentioned baroclinic wave life cycle, the 3D frontal development is noticeably different from that in the semigeostrophic solution (Rotunno et al. 1994). As reargued by Hoskins (2003), however, it is a mostly reliable model for conservative, strictly 2D, deformation-flow frontogenesis. Even in 2D frontogenesis, however, simulations show late-time deviations from semigeostrophy, albeit not primarily as radiating gravity waves (Snyder et al. 1993).

The concept of an approximate force balance with small residual acceleration is relevant for many geophysical flows influenced by Earth's rotation and stable density stratification. Quasi-geostrophy is an extreme balance approximation (as $Ro \to 0$), with approximate geostrophic and hydrostatic momentum balances. Semigeostrophy is a somewhat more general balance approximation, but as noted above, it is not asymptotically consistent in Ro. A consistent higher-order balance approximation, but still based on $|\delta|/|\zeta| \lesssim 1$, is the Balance Equations introduced by Lorenz (1960); they have been shown to be often accurate even for $Ro \sim 1$ up to the limits of their time integrability, which often coincide with the onset of instabilities or inertia–gravity wave radiation whose force and acceleration relations are clearly unbalanced (McWilliams et al. 1998).

The simulation evidence is that gravity wave radiation is usually weak in frontogenesis, except sometimes for gravity fronts (Section 3.3). This suggests that the dynamics is mostly force balanced. Furthermore, a balance model is a partial differential equation system with fewer time derivatives than in the more primitive dynamics, and for many such models, including semigeostrophy and the Balance Equations, a single field is a sufficient initial condition to determine all fields, including the instantaneous time derivatives. This leads to the concept of a secondary circulation and frontogenetic tendency (SCFT) diagnostic analysis. SCFT analysis is a generalization for finite Ro of the omega and Sawyer–Eliassen equations for w and Ψ^y in Equations 10 and 12 to determine the full velocity $\mathbf{u}$ field for specified buoyancy b and hydrostatic pressure ϕ fields, and then an evaluation with $\mathbf{u}$, b, and ϕ of the general frontogenetic tendencies $\mathcal{T}^b$ and

$\mathcal{T}^u$ in Equations 2 and 5, also including other nonconservative effects as relevant. Most balanced models are expressed as a coupled, nonlinear, multivariate partial differential equation system, and as such they may require inversion of elliptic operators or even iteration among the component equations at a given time; furthermore, these inversions or iterations can be expected to fail at a sufficiently large *Ro* value (McWilliams et al. 1998). This implies that balanced models may not be completely accurate or even have exact solutions for very strong fronts; nevertheless, they can be very accurate for a moderate *Ro* value and often do seem to have approximate validity even for a large *Ro*.

The Balance Equations are an appropriate SCFT model for strong 3D frontogenesis due to a larger-scale deformation field (Section 3.1), and the boundary-layer vertical-mixing terms need to be included in an SCFT analysis for strong TTW frontogenesis (Section 3.2). Balance models are probably inapt for gravity-steepening frontogenesis because the acceleration rates are large, and an SCFT analysis may not be meaningful.

A canonical situation in the ocean for deformation frontogenesis is along the separated western boundary currents, e.g., the Gulf Stream and Kuroshio (as well as the atmospheric jet stream). These are strong eastward jets, and they develop sharp surface fronts on their poleward edge, with a narrow width (<5 km) compared with the width of the jet as a whole (≈50 km) (Klymak et al. 2016). These jets often meander around their central latitude with a downstream wavelength of ≈400 km. Because of these meanders, an omega equation (Equation 10) solution indicates a downward w on the downstream faces (i.e., sectors between a crest and the neighboring trough to the east) and upward w on the upstream faces. They have *Ro* values that are not small, so a quasi-geostrophic analysis is inaccurate.

The results from a Balance Equation SCFT analysis of an idealized meandering jet are shown in **Figure 5**. This figure posits a $b(\mathbf{x})$ structure mimicking measured and simulated Gulf Stream fields. Besides the implied surface-intensified eastward jet $u_g(y, z)$ and the meanders, further assumptions are made about its variable width (narrower in troughs), meridional asymmetry (sharper b_y on the poleward side), and tilted vertical structure (the jet center shifts equatorward with depth). All of these attributes influence the SCFT outcome, mostly in a way that concentrates the strongest interior w near the trough and has large, positive values of $\mathcal{T}^b$ and $\mathcal{T}^u$ on the polar side of the downstream face, with negative values along the upstream face. This implies frontogenesis along the polar wall going from the crest to the trough, and a relaxation (frontolysis) from trough to crest. The frontogenesis and secondary circulation would be absent without the meanders that provide a deformation field acting on the different sectors. The situation in **Figure 5** has a symmetric b shape on the up- and downstream faces of the meander, so the diagnosed w and $\mathcal{T}$ fields are antisymmetric with respect to the trough; accounting for a narrower front on the downstream face would give a further positive feedback in $\mathcal{T}$, so it would sharpen even more there. In this example, with a $b(\mathbf{x})$ that has a realistic shape and amplitude, the finite-*Ro* SCFT solution has sizable fraction corrections to the quasi-geostrophic SCFT solution that overestimates $\mathbf{u}_a$ and $\mathcal{T}$. In simulations and measurements of the real Gulf Stream, these SCFT patterns are qualitatively confirmed, together with the observed behaviors of outbreaks of submesoscale instabilities and detaching thermal streamers along the polar wall on the relaxing upstream face and crest, and their suppression on the frontogenetic downstream face and trough (Klymak et al. 2016, McWilliams et al. 2019).

Under the assumptions of $u_a^i \sim Ro\, u_g^i$ and of horizontal anisotropy in $b_{,i}$ (i.e., frontality), a scaling analysis as $Ro \gtrsim 1$ for the Lagrangian frontogenetic tendency equations yields the result that the controlling rate is the convergence itself:

$$\mathcal{T}^b \approx -\delta(b_{,i}b_{,i}), \qquad \mathcal{T}^u_{ad} + \mathcal{T}^u_\phi \approx -\delta\left[(u^j_{,i}u^j_{,i}) + f\zeta_a\right], \qquad 25.$$

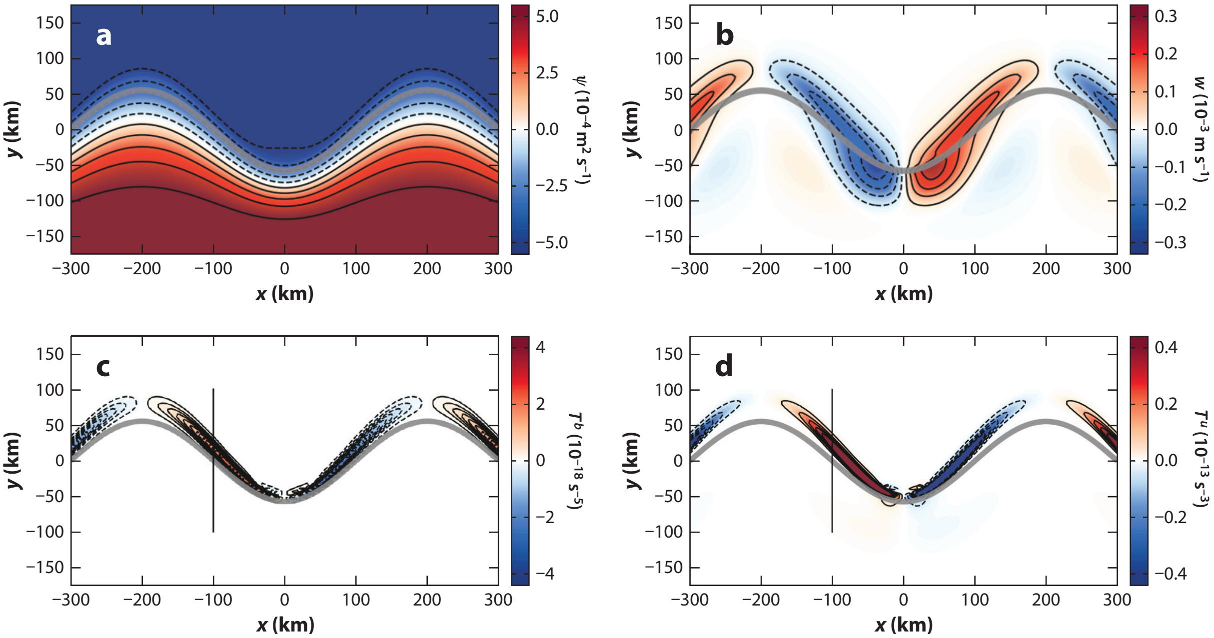

Figure 5

Analysis of the secondary circulation and frontogenetic tendencies for an idealized buoyancy field representing a meandering, surface-intensified, eastward jet with a relatively narrow polar shear zone and trough sector and an equatorward tilt of the jet center position with depth, based on the Balance Equations: (*a*) rotational streamfunction at the surface ψ, (*b*) w at 100-m depth, and (*c*,*d*) $\mathcal{T}^{b,u}$ at the surface. The gray line is the jet center defined as the maximum downstream velocity at the surface (McWilliams et al. 2019).

with $\zeta_a = \epsilon_{zij} u^j_{a,i}$ the ageostrophic vertical vorticity. The associated estimate for energy conversion is $wb \sim fV^2$ (cf. Equations 14 and 19). Furthermore, the Lagrangian tendency equations for the vorticity and divergence are

$$\frac{D\zeta}{Dt} \approx -\delta(\zeta + f), \qquad \frac{D\delta}{Dt} \approx -\delta^2 + f\zeta_a \qquad 26.$$

(Barkan et al. 2019). This has the general implication that frontogenesis, as captured in these approximate equations, becomes a runaway process once $Ro \gg 1$. Treating these equations as ordinary differential equations in time in the Lagrangian frame, the asymptotic solutions for all these quantities are $\propto [1 + \delta_0(t - t_0)]^{-1}$ for $t \geq t_0$ and $\delta(t_0) = \delta_0$. Thus, strong frontogenesis occurs for $\delta < 0$ (i.e., convergence), and it tends toward a finite-time singularity at $t_s = t_0 - \delta_0^{-1}$. For $Ro \sim 1$, the time period is several hours. This model is particularly apt for TTW frontogenesis where $Ro \sim Ek$ at early time (Section 3.2), and the correlation between $-\delta$ and $\mathcal{T}^{u,b}$ is confirmed for the simulation in **Figure 6**. It indicates that there is a late stage of frontogenetic behavior that is independent of the initiating process—subject to disruption, of course, if the assumed frontal anisotropy is broken by other processes, such as instability, turbulence, or wave radiation.

During strong surface frontogenesis, the vorticity ζ grows apace with $|b_{,i}|$, δ, and w. Furthermore, their probability density functions develop long tails, expressing intermittency, and they also exhibit significant skewness, positive for ζ/f (cyclonic) and negative for δ (convergence) and w (downwelling); i.e., frontogenesis with finite Ro is dominated by strong surface convergence, upper-ocean downwelling, and cyclonic vorticity (McWilliams 2016, Barkan et al. 2019). The

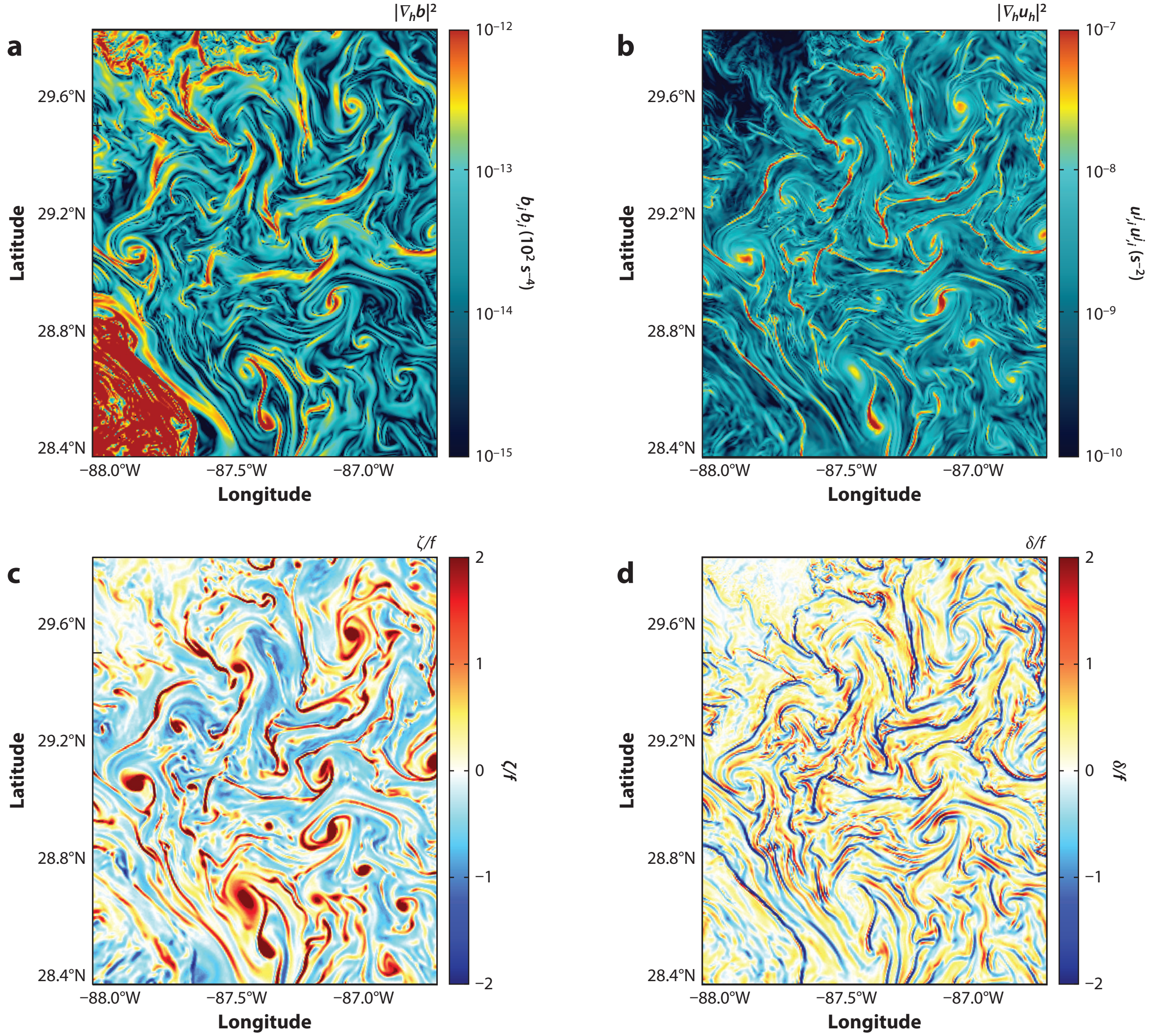

Figure 6

Snapshot of surface fields in the northern Gulf of Mexico in winter in a hindcast simulation with a horizontal grid resolution of 500 m. The fields are (*a*) $b_{,i}b_{,i}$, (*b*) $u^j_{,i}u^j_{,i}$, (*c*) ζ/f, and (*d*) δ/f. This displays the quasi-homogeneous, closely packed patterns of submesoscale fronts, filaments, and vortices. (The saturated colors in the lower left of panel *a* are where the Mississippi River plume is intruding.) Figure adapted from Barkan et al. (2019).

frontal downwelling is accompanied by horizontal divergence in the oceanic interior, and this provides an advective pathway for subduction of surface-layer waters into the more stratified layers below (Spall 1995, Thomas 2008).

For the most part, simulations have not shown high inertia–gravity wave generation during frontogenesis events, which seem to be mostly force balanced (Snyder et al. 1993). These waves can be emitted, however, when the background strain rate α is large enough or rapidly varying in time, and then remain trapped near the front (Shakespeare & Taylor 2014, 2015). Furthermore, in the presence of near-inertial waves, energy exchanges can occur between the waves and frontal flow (Thomas 2017).

Additionally, surface gravity wave interaction with the fronts occurs due to the wave-averaged effects of Stokes drift $\mathbf{u}^{St}$ through the vortex force, $\mathbf{u}^{St} \times (f\hat{\mathbf{z}} + \nabla \times \mathbf{u})$, and buoyancy advection, $\mathbf{u}^{St} \cdot \nabla b$. These wave–current interaction effects are well understood as the primary dynamical process for surface-layer Langmuir circulations, but in the context of fronts, this is still a new subject area, with as yet only a few simulations and few detailed measurements. The evidence is that surface waves can significantly influence frontogenetic evolution (McWilliams & Fox-Kemper 2013, Suzuki et al. 2016, McWilliams 2018, Sullivan & McWilliams 2019), more by modulating the frontal shapes and rates than by simply negating or amplifying the frontogenesis.

3.5. Frontal Instability, Turbulence, Arrest, and Decay

In the context of 2D semigeostrophic frontogenesis, the question arises, What intervenes to stop a finite-time singularity from occurring? Snyder et al. (1993) addressed this using 2D simulations, and their answer is that nothing does, apart from grid-scale diffusion. More realistically, with large Reynolds numbers, it is likely that some 3D frontal instability develops that overtakes the frontogenesis as the frontal velocity gradient amplifies, grows into finite amplitude frontal eddies, and provides arresting eddy momentum or buoyancy fluxes at some finite scale larger than a molecular diffusion length. This is well known for gravity bores with their churning, turbulent faces, but it has been less clear for more rotationally influenced fronts. Many types of shear instability are possible, and maybe different types occur under different circumstances.

One oceanic paradigm is baroclinic instability of surface frontogenesis when *Ro* is not large. Spall (1997) simulated frontal evolution in a confluent deformation flow and showed a baroclinic eddy arrest when α is relatively small, but the instability is suppressed for larger α values. In a theoretical 3D stability analysis of 2D deformation frontogenesis, the eddy growth rate amplifies as the front sharpens until it exceeds the frontogenetic rate, and a tendency develops toward frontal arrest, at least within a Galerkin wavenumber truncation (McWilliams et al. 2009b, McWilliams & Molemaker 2011).

A related paradigm is the baroclinic instability of a quiescent surface frontal zone that is not undergoing active frontogenesis. In a weakly stratified surface layer, this is called mixed-layer instability, and 3D perturbations amplify into mixed-layer eddies that themselves develop secondary deformation fronts on their edges (Fox-Kemper et al. 2008), somewhat analogous to the baroclinic wave life cycle in the jet stream (Section 3.4). This situation of the spin-down of the primary baroclinic front has been simulated in detail with Large Eddy Simulations (Hamlington et al. 2014, Samelson & Skyllingstad 2016, Verma et al. 2019).

Besides the small *Ro* instability types (i.e., baroclinic or barotropic shear instabilities, depending on whether the background $fu^i_{,z}/N$ or $u^i_{,y}$ is the dominant fluctuation energy source), other types become available at larger *Ro* values. These types include (*a*) Kelvin–Helmholtz for small Richardson numbers, $Ri = N^2/(u^i_{,z})^2$ (instability of the vertical shear of the horizontal current in a stably stratified layer); (*b*) centrifugal or symmetric when the Ertel potential vorticity,

$$q = (f\hat{\mathbf{z}} + \nabla \times \mathbf{u}) \cdot \nabla b, \qquad 27.$$

has a different sign from f (a small-scale instability of either vertical or horizontal shear, depending on the stratification strength); and (*c*) gravitational when $b_{,z} < 0$ (convection when heavy fluid overlies light) (Haine & Marshall 1998)—and possibly other types not yet commonly identified.

Apart from the instability thresholds implicit in the frontal shear profiles, air–sea fluxes of momentum and buoyancy can change the local sign of q in a front and trigger symmetric instability (Thomas & Lee 2005, Taylor & Ferrari 2009).

In spite of all the attention given in the meteorological community to the expectation of frontal collapse (Hoskins 2003), remarkably little is known about the outcome of strong frontogenesis events that proceed to a very-small-width ℓ, either in measurements or in simulations. The difficulty is the enormous range of spatial scales involved.

The fate of frontogenesis has been recently assessed through simulations of an isolated, dense-surface-filament TTW frontogenesis event using a Large Eddy Simulation model (Sullivan & McWilliams 2018). Starting from an initial loosely constrained $\langle b \rangle(x, z) \propto \langle \theta \rangle(x, z)$ (where $\langle \cdot \rangle$ denotes an along-front average) in a state of otherwise fully developed turbulence and with a partially adjusted frontal velocity $\langle \mathbf{u} \rangle(x, z)$, the flow is released for free evolution at $t = 0$. The boundary-layer turbulence is sustained by surface cooling (i.e., convection). Its presence causes TTW frontogenesis of the filament (Section 3.2).

The initial $\langle \mathbf{u} \rangle(x)$ and $\langle \theta \rangle(x)$ profiles at the surface are shown in **Figure 7*b*,*c*** (dashed lines). The initial frontal width is $\ell \approx 2$ km, and over the course of the next 6 h it collapses to a width of $\ell \approx 50$ m (comparable to the boundary-layer depth), when it becomes arrested from further sharpening. During that time, peak values of the horizontal gradients—$\langle \delta \rangle = \langle u \rangle_{,x}$, $\langle \zeta \rangle = \langle v \rangle_{,x}$, and $\langle \theta \rangle_{,x}$—increase by more than an order of magnitude, while the horizontal velocities increase more modestly (**Figure 7**). The peak value of $\langle \zeta \rangle / f \approx 120$ is a local maximum estimate for *Ro*; i.e., the dynamics has become extremely ageostrophic. Underneath the surface front, the minimum $\langle w \rangle$ is also very large, more than 0.02 m s^{-1}. The turbulent kinetic energy, $TKE = \langle \mathbf{u}'^2 \rangle / 2$, also increases more than 100-fold over its ambient value in the far-field homogeneous convection. Thus, turbulent mixing and dissipation are greatly amplified inside an active front.

Velocity sections $\langle \mathbf{u} \rangle(x, z)$ through the filament core at the time of frontal arrest (**Figure 8**) still show the characteristic patterns of TTW frontogenesis (cf. **Figure 3**), even though the frontal dynamics is much more advective than it is in the simple linear balance (Equation 16). Even after the full frontogenetic period, the density extremum at the surface is only slightly reduced from its initial value. The frontal vorticity $\langle \zeta \rangle$ and turbulent kinetic energy *TKE* are highly concentrated in the center and near the surface. Furthermore, the horizontal Reynolds stress is strongly negative through the core of the frontal gradient region. The sign of this stress expresses a horizontal shear instability, with a positive frontal eddy generation rate, $-\langle u'v' \rangle \langle v \rangle_{,x} > 0$, and is the agent of frontal arrest by mean momentum flux across the filament. After peak arrest, a prolonged period (days) of frontal decay ensues, with TTW frontogenesis working against eddy momentum flux arrest; meanwhile, $\langle w \rangle \, \langle b \rangle > 0$ continues to extract available potential energy from the upper-ocean buoyancy field, and a high dissipation rate is maintained by the forward cascade of *TKE* from the filament currents. The 3D wavenumber spectrum is continuous between the submesoscale frontal instability and the boundary-layer turbulence; i.e., once generated by the instability, the kinetic energy cascades directly to microscale viscous dissipation. In other cases with wind-stress generation of the vertical-momentum mixing, the TTW secondary circulations are asymmetric across the filament in combination with Ekman currents; in these cases, the particular frontal behaviors vary substantially with the direction of the wind relative to the frontal axis (Thomas & Lee 2005, Sullivan & McWilliams 2018).

This event can be seen as a paradigm for a nongravitational frontal life cycle, whether by a persistent background deformation field or by sustained vertical-momentum mixing, and whether for a surface front or filament. Its particular type of arresting frontal instability is likely not universal.

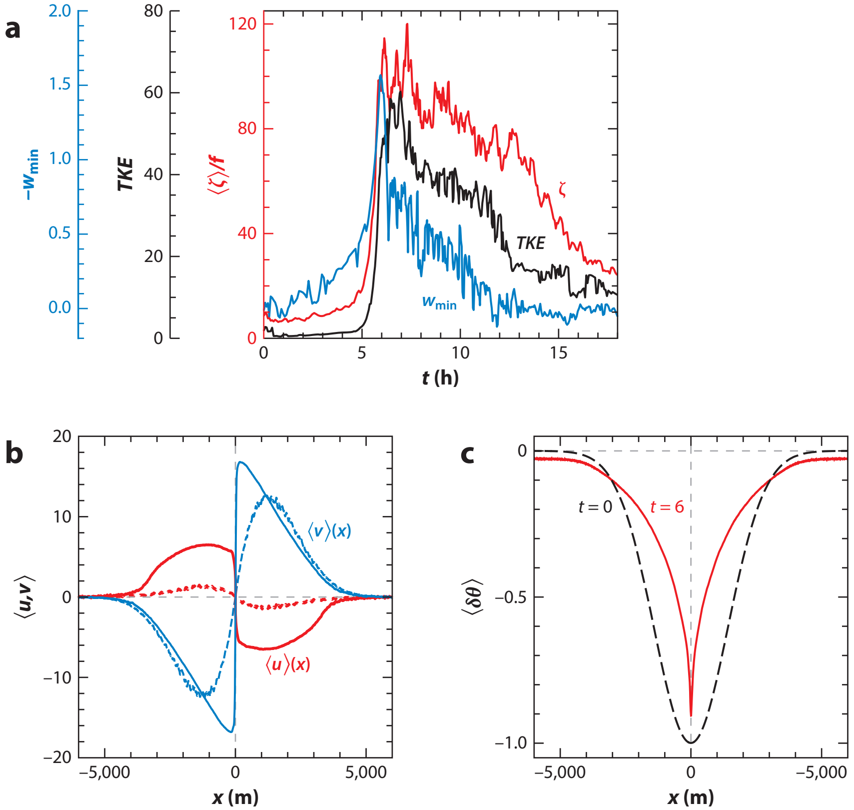

Figure 7

(*a*) Time series of peak along-front-averaged, normalized values in the center of a cold-filament frontogenesis event in a Large Eddy Simulation model with turbulence generated by surface cooling: surface vertical vorticity $\langle\zeta\rangle(t)/f$, interior downwelling velocity $\langle w\rangle(t)/w_*$ (where w_* is the convective-forcing velocity scale), and surface turbulent kinetic energy $\langle TKE\rangle(x)/w_*^2$ for deviations from the along-front-averaged currents. (*b*,*c*) Along-front-averaged, cross-front, surface profiles of normalized $\langle u\rangle(x)$ (*red*) and $\langle v\rangle(x)$ (*blue*) (panel *b*) and temperature (buoyancy) anomaly $\langle\delta\theta\rangle(x)$ (panel *c*); normalizations are by w_* and the initial peak value of $|\langle\delta\theta\rangle| = 0.5°C$ in the filament center at the surface. Profiles at $t = 0$ are dashed lines, and those at $t = 6$ h are solid lines. Frontogenesis is dominant at early time. Frontal arrest occurs at approximately $t = 6$ h, and then a slower decay period ensues. Figure adapted from Sullivan & McWilliams (2018).

4. FRONTAL PHENOMENA

Fronts of many types are found in many places in the ocean, especially at the surface (**Figure 9**). In this section, a brief survey is made of some of the more familiar types, although no claim is made for comprehensiveness, and only a few sample references are included.

4.1. Climatological Fronts

Ocean observers have long known of semipermanent fronts in a variety of locations. These fronts can be due to current edges, Ekman transport convergences, water-mass boundaries, and bathymetric influences. Examples are the polar edges of separated western boundary currents (**Figure 5**), the zonal subpolar and subtropical fronts in the Atlantic and Pacific (Roden 1980, Rudnick & Luyten 1996), the Mediterranean salinity front (Tintore et al. 1988) (see also

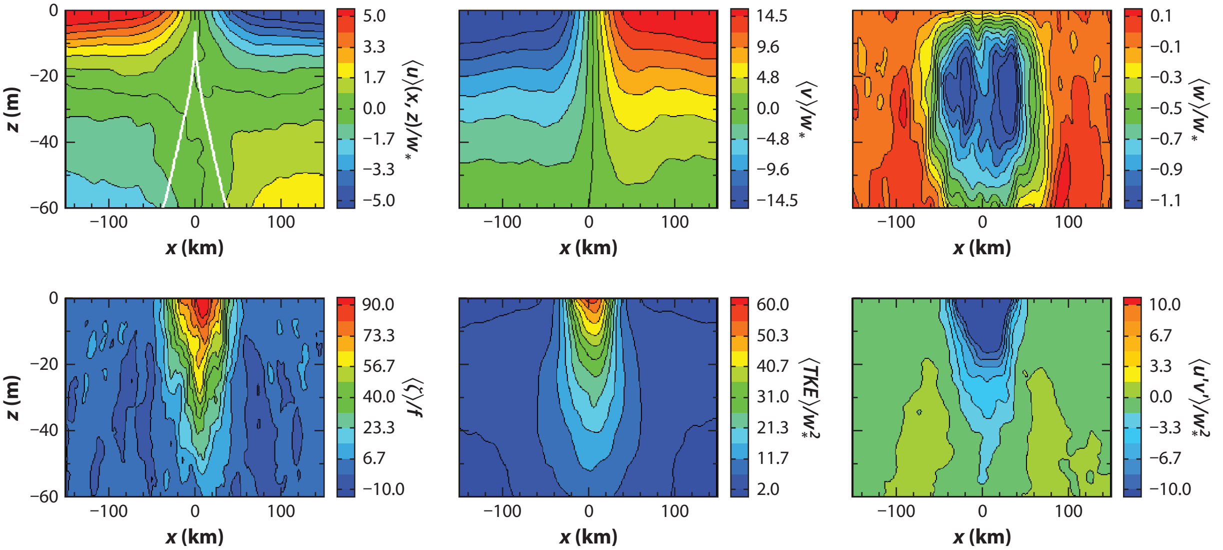

Figure 8

Along-front-averaged sections in the dense-filament frontogenesis event in **Figure 7** at the time of peak frontal strength ($t = 6$ h). (*Top row*) $\langle u \rangle(x, z)$, $\langle v \rangle$, and $\langle w \rangle$ normalized by w_*. (*Bottom row*) $\langle \zeta \rangle / f$, $\langle TKE \rangle / w_*^2$, and horizontal Reynolds stress $\langle u'v' \rangle / w_*^2$ (with prime a deviation from the along-front average $\langle \cdot \rangle$). This last field is the horizontal eddy momentum flux arising from frontal shear instability, whose divergence arrests the frontogenesis caused by the averaged secondary circulation. The white line on the u plot (*upper left*) is the position of the normalized anomaly isotherm $\langle \delta\theta \rangle = -0.87$ at this time. Figure adapted from Sullivan & McWilliams (2018).

Figure 10), and multiple zonal fronts in the Antarctic Circumpolar Current (Sokolov & Rintoul 2009). Temperature and salinity fronts are usually density fronts, but sometimes they are density compensated, with only a water-mass gradient. Boundary upwelling currents from offshore Ekman transport exhibit strong cross-shore surface T gradients (e.g., off California), but their overturning

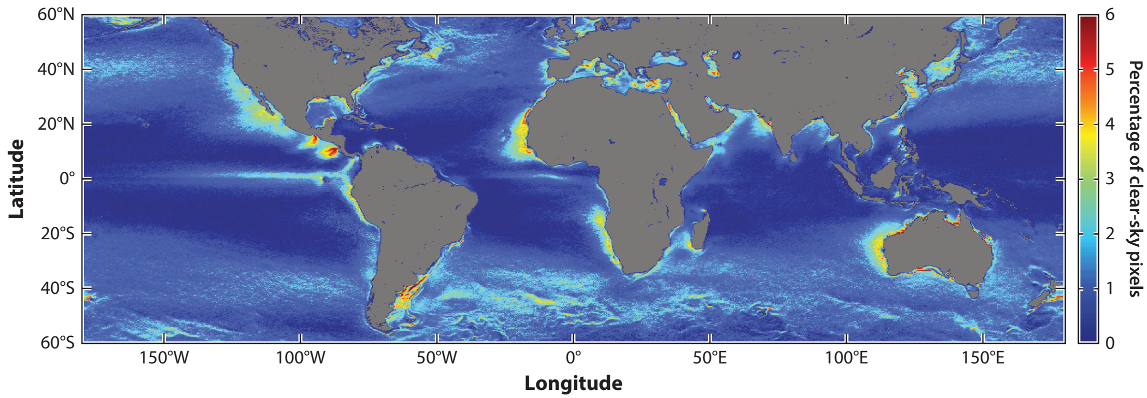

Figure 9

Probability (percentage of clear-sky pixels) of finding a sea-surface temperature front based on the satellite radiometry Advanced Very-High-Resolution Radiometer (AVHRR) Pathfinder 4-km data set, processed with the Cayula–Cornillon algorithm. Fronts are sparse but not uncommon, especially near coasts, where the currents are often stronger and some fronts are semipermanent in relation to bathymetry. Many fronts are too narrow to be detected with this data set. Figure adapted from Y. Mauzole & P. Cornillon (manuscript in preparation).

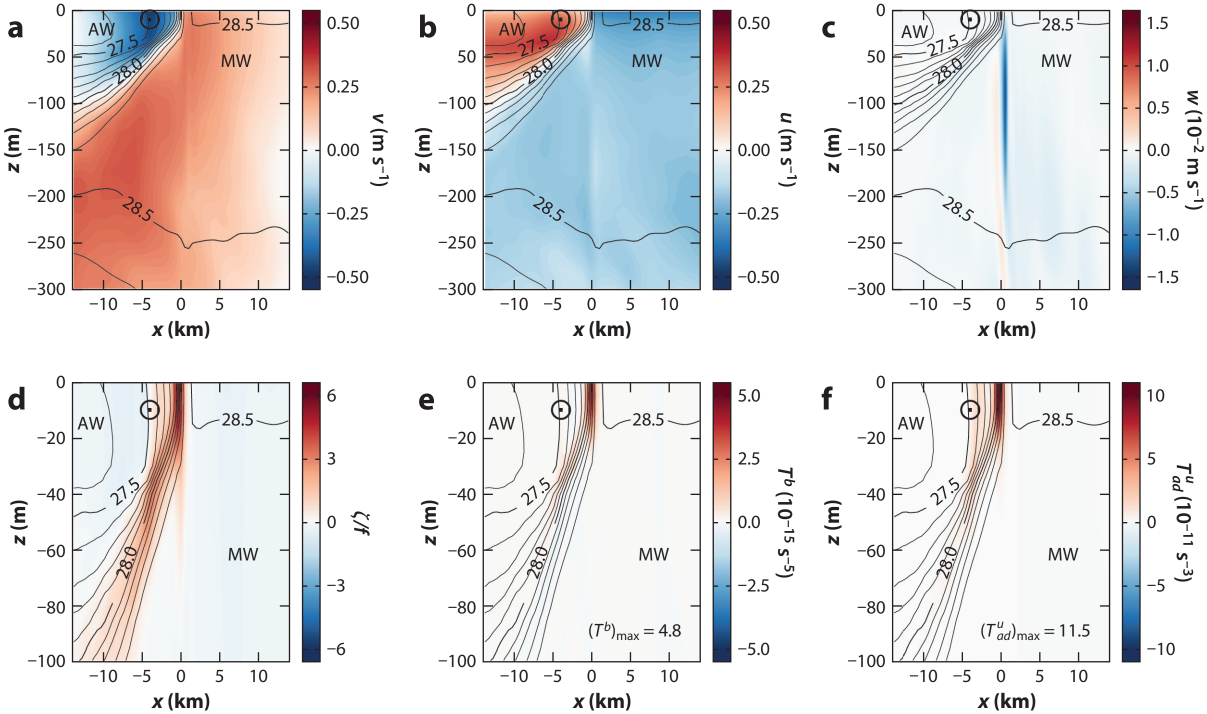

Figure 10

Zonal (x, z) sections across the Almeria–Oran front in the western Mediterranean Sea at 2.7°W, 36.3°N, averaged over a frontogenetic event on March 10–11, 2011, in a hindcast simulation with a horizontal grid resolution of 500 m. The fields are (*a*) v, (*b*) u, (*c*) w, (*d*) ζ/f, (*e*) $\mathcal{T}^b$, and (*f*) $\mathcal{T}^u_{ad}$. The event shows a strong secondary circulation and $\mathcal{T}^{b,u} > 0$. This front recurrently lies between the climatological surface water masses of fresh Atlantic water (AW) and salty Mediterranean water (MW), and it exhibits episodes of frontogenesis and relaxation depending on the neighboring flow patterns. Light black isolines of density show strong stratification on the western (light) side. The circle with a dot denotes the southward, along-front flow at the surface. Notice the vertical range change between top and bottom rows. Figure adapted from E. Capo & J.C. McWilliams (manuscript in preparation).

circulation is usually divergent at the surface; however, the persistence of this front opens the possibility of frontogenetic episodes.

4.2. Deformation Fronts

Deformation fronts occur where the background strain field is favorably aligned with surface $b_{,i}$ for frontogenesis (Section 3), e.g., in confluent flows near separating boundary currents, in meanders along mid-oceanic jets (**Figure 10**), or around the edge of mesoscale eddies. During frontogenesis events, the local *TKE*, tracer mixing, and energy dissipation can be quite strong (Nagai et al. 2009, D'Asaro et al. 2011).

4.3. Submesoscale Fronts

Submesoscale fronts and dense filaments—and their coherent vortex instability products—are quite common at the oceanic surface, especially during periods where the weakly stratified surface boundary layer is thick (e.g., **Figure 6**). This subject has been covered in previous reviews (McWilliams 2016, 2019), where many relevant references are listed. Their energy source is the available potential energy in near-surface $b_{,i}$ (Section 3). The TTW generation process is frequently important (Section 3.2) (Thompson 2000, Gula et al. 2014, McWilliams et al. 2015, McWilliams 2017, Bodner et al. 2020), and it exhibits very strong surface convergence, $\delta < 0$ (D'Asaro et al. 2018, Barkan et al. 2019), as well as primarily cyclonic vorticity generation, $\zeta/f > 0$. Submesoscale fronts and dense filaments are the most effective agents of lateral spreading of materials in the intermediate patch-size range of 10^2–10^4 m, while also locally and temporarily inhibiting spreading through convergence and downwelling (D'Asaro et al. 2018, Dauhajre et al. 2019). A diurnal modulation cycle of frontogenesis and relaxation occurs as solar heating modulates the boundary-layer turbulence mixing rate, $\nu(\mathbf{x}, t)$ (Dauhajre & McWilliams 2018).

4.4. Gravity Fronts

Gravity fronts happen in the ocean wherever an unbalanced, large-amplitude, gravity-steepening dynamics is dominant (Section 3.3). Besides the familiar surface-interfacial phenomena of breaking waves, shoaling tidal bores, and tsunamis, interior gravity fronts arise from river inflows, often influenced by tidal pulsing (Garvine 1974, Horner-Devine et al. 2015, Akan et al. 2018); from shoaling internal tides (Lamb 2014); and from dense-water overflows through straits or over sills (Spall et al. 2019). As these interior density fronts propagate over a time interval $\sim 1/f$, they transition from $|\delta| \gg |\zeta|$ by increasing the along-front velocity until these quantities become more comparable, weaken the horizontal density anomaly through vertical mixing, and slow down.

Figure 11 shows the generation of an internal tidal bore incident on a shoaling oceanic coast. In this particular case, dependent on the vertical stratification and topographic profiles, there is a

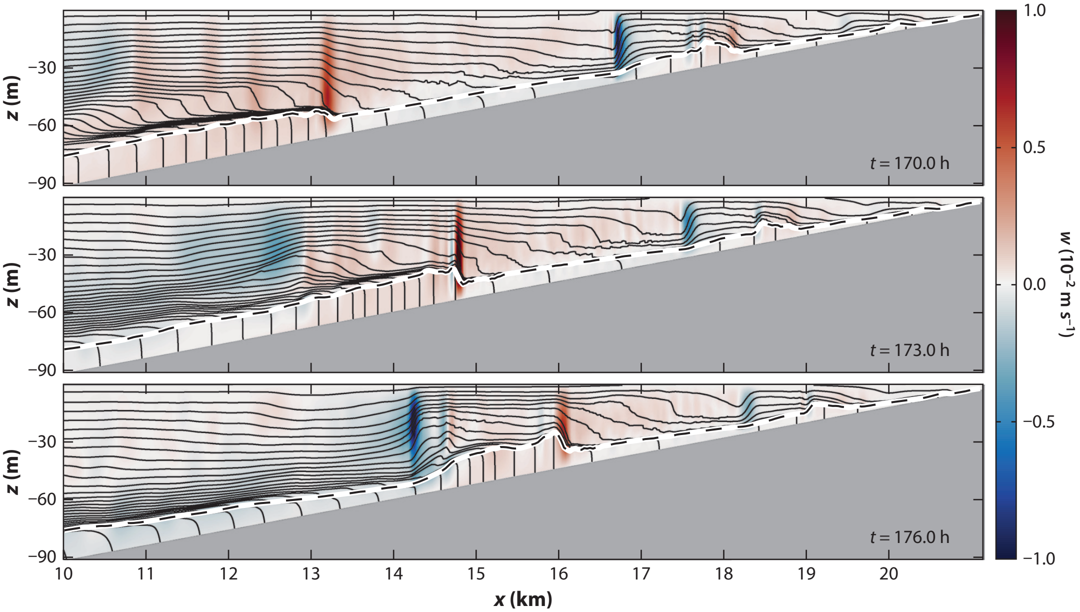

Figure 11

Successive snapshots from an idealized process simulation of a shoaling M2 internal tide on the continental shelf. Contours are isolines of buoyancy b, and colors are vertical velocity w. The dashed line indicates the top of the turbulent bottom boundary layer with parameterized mixing. As the waves progress shoreward, frontogenesis and bore formation occur both on the forward face with bottom-initiated upwelling and on the rear face with interior-induced downwelling, while also slowing in propagation speed. Close to shore, the waves weaken and dissipate. Figure adapted from D. Dauhajre, J.C. McWilliams & M.J. Molemaker (manuscript in preparation).

double bore per tidal cycle; one forms from a wave of isopycnal elevation on the leading forward face, and the other forms from a wave of depression on the trailing rear face (a similar behavior is also shown in Lamb & Warn-Varnas 2015). The associated frontal vertical velocities are of opposite sign: upward on the elevation wave face and downward behind. As a result, the local potential–kinetic energy exchange $w'b'$ is opposite in the two bores; it is almost entirely a redistribution of energy within the wave field itself, as in a propagating linear internal wave. This is one of several ways that gravity frontogenesis is different from more rotationally influenced frontogenesis.

4.5. Topographic Fronts

Where currents adjacent to the bottom encounter an abrupt topographic change, flow separation can occur with associated density fronts, through either convergence or geostrophic adjustment to the strong vorticity generation by drag against the boundary. A conspicuous example is bottom fronts at the topographic shelf–slope boundary (Gawarkiewicz & Chapman 1992, Chapman 2000), and they can also manifest at the surface (Wang & Jordi 2011). Furthermore, surface fronts are also often visible as current edges separating from coastal headlands or islands.

4.6. Vertical Mixing Fronts

In shallow stratified water, tidally induced vertical buoyancy mixing can generate a top-to-bottom, shore-parallel density front with a dipole secondary circulation with surface convergence (Hill et al. 1993, Loder et al. 1993, van Heijst 1986). A similar phenomenon can occur at the edge of a strongly mixing surf zone with stratified offshore water (P. Wang, manuscript in preparation).

4.7. Estuarine Fronts

Estuaries are shallow, semienclosed basins surrounding river mouths. They are characterized by strong S gradients between the river and the sea, and they often form into fronts (Geyer & Ralston 2015) through all of the processes mentioned in Sections 4.4–4.6, particularly in association with strong tidal currents.

4.8. Frontal Air–Sea Interaction

Oceanic fronts provide oceanic surface temperature T and velocity $\mathbf{u}$ gradients for the air–sea fluxes of momentum, heat, moisture, and soluble gases, which in turn induce gradients in the flux (Friehe et al. 1991, Baschek et al. 2006). These gradients have several significant effects in the lower atmosphere and upper ocean. The T gradient modifies the buoyant stability (stratification) of the lower atmosphere, with a weaker stability, deeper boundary layer, and stronger surface wind on the warm side. This induces a gradient in the surface stress, i.e., causing stress divergence for cross-front winds and stress curl for along-front winds (Small et al. 2008, Gaube et al. 2019). This further generates secondary circulations both in the atmospheric boundary layer, sometimes extending to its top (Sullivan et al. 2020), and in the oceanic Ekman-layer currents and vertical-velocity pumping. Another significant effect is associated with $\mathbf{u}$ gradients that modulate the surface stress that is a function of the air–sea relative velocity difference. This, in turn, both modifies the adjacent Ekman winds and currents and induces a large sink of oceanic eddy kinetic energy transferred back into the atmosphere (Renault et al. 2018).

5. SUMMARY

Horizontal density fronts occur frequently in the ocean, especially at the surface, the bottom, and near the shore, while the abundance and strength of fronts in the interior is less well known. In favorable circumstances of deformation flow, horizontal convergence, or vertical-momentum and buoyancy mixing, the fronts can sharpen rapidly through frontogenesis. The frontal width can be arrested by the cessation of the frontogenetic agency, by frontal instability, or by horizontal mixing.

Fronts perform many important oceanic system functions. In energy, they extract available potential energy from horizontal density gradients and facilitate the transfer of kinetic energy to small-scale mixing and dissipation. In the weakly stratified surface layer, they act to increase the stratification against the action of boundary-layer turbulence, and they induce material exchanges with the more stratified interior. They enhance lateral dispersion of material overall but locally inhibit it through surface convergences of buoyant material. They modulate air–sea interactions through both their surface T and $\mathbf{u}$ horizontal gradients. They broach the boundary of the geostrophic dynamics that prevails for most larger-scale currents. These functions must be represented in the oceanic system as a whole, i.e., in circulation and biogeochemical models for mesoscale, basin, and planetary flows and material distributions.

The past decade has shown a flowering of interest in oceanic fronts, their life cycles, and their impacts. Yet it seems quite likely that there is much still to learn about the variety of their manifestations. They pose a difficult measurement challenge with their multidimensional scale breadth and their rapid evolution. They do emerge spontaneously in circulation models with sufficient spatial resolution, and Large Eddy Simulation models are powerful tools for their fuller depiction, albeit at a high computational cost. The nature of the arresting processes and the interaction of fronts with their concomitant small-scale turbulence are at the frontiers of our scientific understanding of these phenomena.

DISCLOSURE STATEMENT

The author is not aware of any affiliations, memberships, funding, or financial holdings that might be perceived as affecting the objectivity of this review.

LITERATURE CITED

Akan C, McWilliams JC, Moghimi S, Ozkan-Haller HT. 2017. Frontal dynamics at the edge of the Columbia River plume. *Ocean Model.* 122:1–12

Barkan R, Molemaker MJ, Srinivasan K, McWilliams JC, D'Asaro E. 2019. The role of horizontal divergence in submesoscale frontogenesis. *J. Phys. Oceanogr.* 49:1593–618

Baschek B, Farmer DM, Garrett C. 2006. Tidal fronts and their role in air-sea gas exchange. *J. Mar. Res.* 64:483–515

Benjamin TB. 1966. Internal waves of finite horizontal amplitude and permanent form. *J. Fluid Mech.* 25:241–53

Benjamin TB. 1968. Gravity currents and related phenomena. *J. Fluid Mech.* 31:209–48

Bjerknes J. 1919. On the structure of moving cyclones. *Geofys. Publ.* 1(2):1–8

Bodner AS, Fox-Kemper B, Van Roekel LP, McWilliams JC, Sullivan PP. 2020. A perturbation approach to understanding the effects of turbulence on frontogenesis. *J. Fluid Mech.* 883:A25

Chapman DC. 2000. Boundary layer control of buoyant coastal currents and the establishment of a shelfbreak front. *J. Phys. Oceanogr.* 30:2941–55

D'Asaro E, Lee C, Rainville L, Thomas L. 2011. Enhanced turbulence and energy dissipation at ocean fronts. *Science* 332:318–22

D'Asaro E, Shcherbina AY, Klymak JM, Molemaker MJ, Novelli G, et al. 2018. Ocean convergence and the dispersion of flotsam. *PNAS* 115:1162–67

Dauhajre D, McWilliams JC. 2018. Diurnal evolution of submesoscale front and filament circulations. *J. Phys. Oceanogr.* 48:2343–61

Dauhajre D, McWilliams JC, Renault L. 2019. Nearshore Lagrangian connectivity: submesoscale influence and resolution sensitivity. *J. Geophys. Res. Oceans* 124:5180–204

Davies HC. 1999. Theories of frontogenesis. In *The Life Cycles of Extratropical Cyclones*, ed. MA Shapiro, S Gronas, pp. 215–38. Boston: Am. Meteorol. Soc.

Federov KN. 1986. *The Physical Nature and Structure of Oceanic Fronts*. New York: Springer-Verlag

Ferrari R, Rudnick DL. 2000. Thermohaline variability in the upper ocean. *J. Geophys. Res.* 105:16857–83

Fox-Kemper B, Ferrari R, Hallberg R. 2008. Parameterization of mixed layer eddies. Part I: theory and diagnosis. *J. Phys. Oceanogr.* 38:1145–65

Friehe CA, Shaw WJ, Rodgers DB, Davidson KL, Large WG, et al. 1991. Air-sea fluxes and surface layer turbulence around a sea surface temperature front. *J. Geophys. Res.* 96:8593–609

Garvine RW. 1974. Dynamics of small-scale ocean fronts. *J. Phys. Oceanogr.* 4:557–69

Gaube P, Chickadel CC, Branch R, Jessup A. 2019. Satellite observations of SST-induced wind speed perturbation at the oceanic submesoscale. *Geophys. Res. Lett.* 46:2690–95

Gawarkiewicz G, Chapman DC. 1992. The role of stratification in the formation and maintenance of shelf-break fronts. *J. Phys. Oceanogr.* 22:753–72

Gent PR, McWilliams JC, Snyder C. 1994. A note on a scaling analysis of curved fronts: the formal validity of the balance equations and semigeostrophy. *J. Atmos. Sci.* 51:160–63

Geyer WR, Ralston FP. 2015. Estuarine frontogenesis. *J. Phys. Oceanogr.* 45:546–61

Gula J, Molemaker MJ, McWilliams JC. 2014. Submesoscale cold filaments in the Gulf Stream. *J. Phys. Oceanogr.* 44:2617–43

Haine TWN, Marshall J. 1998. Gravitational, symmetric and baroclinic instability of the ocean mixed layer. *J. Phys. Oceanogr.* 28:634–58

Hamlington PE, Van Roekel LP, Fox-Kemper B, Julien K, Chini GP. 2014. Langmuir-submesoscale interactions: descriptive analysis of multiscale frontal spindown simulations. *J. Phys. Oceanogr.* 44:2249–72

Hill AE, James ID, Linden PF, Matthews JP, Prandle D, et al. 1993. Dynamics of tidal mixing fronts in the North Sea. *Philos. Trans. R. Soc. Lond. A* 343:431–46

Horner-Devine AR, Hetland RC, MacDonald DG. 2015. Mixing and transport in coastal river plumes. *Annu. Rev. Fluid Mech.* 47:569–94

Hoskins BJ. 1982. The mathematical theory of frontogenesis. *Annu. Rev. Fluid Mech.* 14:131–51

Hoskins BJ. 2003. Back to frontogenesis. In *A Half Century of Progress in Meteorology: A Tribute to Richard Reed*, ed. RH Johnson, RA Houze Jr., pp. 49–59. Boston: Am. Meteorol. Soc.

Hoskins BJ, Bretherton FP. 1972. Atmospheric frontogenesis models: mathematical formulation and solution. *J. Atmos. Sci.* 29:11–37

Hoskins BJ, Draghici I. 1977. The forcing of ageostrophic motion according to the semi-geostrophic equations and in an isentropic coordinate model. *J. Atmos. Sci.* 34:1859–67

Klymak JM, Shearman RK, Gula J, Lee CM, D'Asaro EA, et al. 2016. Submesoscale streamers exchange water on the north wall of the Gulf Stream. *Geophys. Res. Lett.* 43:1226–33

Lamb KG. 2014. Internal wave breaking and dissipation mechanisms on the continental slope/shelf. *Annu. Rev. Fluid Mech.* 46:231–54

Lamb KG, Warn-Varnas A. 2015. Two-dimensional numerical simulations of shoaling internal solitary waves at the ASIAEX site in the South China Sea. *Nonlinear Process. Geophys.* 22:289–312

Lapeyre G, Klein P, Hua BL. 2006. Oceanic restratification forced by surface frontogenesis. *J. Phys. Oceanogr.* 36:1577–90

Loder JW, Drinkwater KF, Oakey NS, Horne EPW. 1993. Circulation, hydrographic structure and mixing at tidal fronts: the view from Georges Bank. *Philos. Trans. R. Soc. Lond. A* 343:447–60

Long RR. 1972. The steepening of long, internal waves. *Tellus* 24:88–99

Lorenz E. 1960. Energy and numerical weather prediction. *Tellus* 12:364–73

Lorenz E. 1969. The predictability of a flow which possesses many scales of motion. *Tellus* 21:289–307

Mahadevan A. 2016. The impact of submesoscale physics on primary productivity of plankton. *Annu. Rev. Mar. Sci.* 8:161–84

McWilliams JC. 2016. Submesoscale currents in the ocean. *Proc. R. Soc. A* 472:20160117

McWilliams JC. 2017. Submesoscale surface fronts and filaments: secondary circulation, buoyancy flux, and frontogenesis. *J. Fluid Mech.* 823:391–432

McWilliams JC. 2018. Surface wave effects on submesoscale fronts and filaments. *J. Fluid Mech.* 843:479–517
McWilliams JC. 2019. A survey of submesoscale currents. *Geosci. Lett.* 6:3
McWilliams JC, Colas F, Molemaker MJ. 2009a. Cold filamentary intensification and oceanic surface convergence lines. *Geophys. Res. Lett.* 36:L18602
McWilliams JC, Fox-Kemper B. 2013. Oceanic wave-balanced surface fronts and filaments. *J. Fluid Mech.* 730:464–90
McWilliams JC, Gent PR. 1980. Intermediate models of planetary circulations in the atmosphere and ocean. *J. Atmos. Sci.* 37:1657–78
McWilliams JC, Gula J, Molemaker MJ. 2019. The Gulf Stream north wall: ageostrophic circulation and frontogenesis. *J. Phys. Oceanogr.* 49:893–916
McWilliams JC, Gula J, Molemaker MJ, Renault L, Shchepetkin AF. 2015. Filament frontogenesis by boundary layer turbulence. *J. Phys. Oceanogr.* 45:1988–2005
McWilliams JC, Molemaker MJ. 2011. Baroclinic frontal arrest: a sequel to unstable frontogenesis. *J. Phys. Oceanogr.* 41:601–19
McWilliams JC, Molemaker MJ, Olafsdottir EI. 2009b. Linear fluctuation growth during frontogenesis. *J. Phys. Oceanogr.* 39:3111–29
McWilliams JC, Yavneh I, Cullen MJP, Gent PR. 1998. The breakdown of large-scale flows in rotating, stratified fluids. *Phys. Fluids* 10:3178–84
Nagai T, Tandon A, Yamazaki H, Doubell MJ. 2009. Evidence of enhanced turbulent dissipation in the frontogenetic Kuroshio Front thermocline. *Geophys. Res. Lett.* 36:L12609
Pedlosky J. 1987. *Geophysical Fluid Dynamics*. New York: Springer-Verlag
Renault L, McWilliams JC, Gula J. 2018. Dampening of submesoscale currents by air-sea stress coupling in the Californian upwelling system. *Sci. Rep.* 8:13388
Roden GI. 1980. On the variability of surface temperature fronts in the western Pacific, as detected by satellite. *J. Geophys. Res.* 85:2704–10
Rotunno R, Skamarock WC, Snyder C. 1994. An analysis of frontogenesis in numerical simulations of baroclinic waves. *J. Atmos. Sci.* 51:3373–98
Rudnick DL, Ferrari R. 1999. Compensation of horizontal temperature and salinity gradients in the ocean mixed layer. *Science* 283:526–29
Rudnick DL, Luyten JR. 1996. Intensive surveys of the Azores Front: 1. Tracers and dynamics. *J. Geophys. Res.* 101:923–39
Samelson RM, Skyllingstad ED. 2016. Frontogenesis and turbulence: a numerical simulation. *J. Atmos. Sci.* 73:5025–40
Shakespeare CJ, Taylor JR. 2014. The spontaneous generation of inertia-gravity waves during frontogenesis forced by large strain: theory. *J. Fluid Mech.* 757:817–53
Shakespeare CJ, Taylor JR. 2015. The spontaneous generation of inertia-gravity waves during frontogenesis forced by large strain: numerical solutions. *J. Fluid Mech.* 772:508–34
Simpson JE. 1997. *Gravity Currents in the Environment and Laboratory*. Cambridge, UK: Cambridge Univ. Press
Simpson JE, Linden PF. 1989. Frontogenesis in a fluid with horizontal density gradients. *J. Fluid Mech.* 202:1–16
Small J, deSzoeke SP, Xie SP, O'Neill L, Seo H, et al. 2008. Air-sea interaction over ocean fronts and eddies. *Dyn. Atmos. Oceans* 45:274–319
Snyder C, Skamarock WC, Rotunno R. 1993. Frontal dynamics near and following frontal collapse. *J. Atmos. Sci.* 50:3194–221
Sokolov S, Rintoul SR. 2009. Circumpolar structure and distribution of the Antarctic Circumpolar Current fronts: 1. Mean circumpolar paths. *J. Geophys. Res.* 114:C11018
Spall MA. 1995. Frontogenesis, subduction, and cross-front exchange at upper ocean fronts. *J. Geophys. Res.* 100:2543–57
Spall MA. 1997. Baroclinic jets in confluent flow. *J. Phys. Oceanogr.* 27:1054–71
Spall MA, Pickart RS, Lin P, von Appen WJ, Mastropole D, et al. 2019. Frontogenesis and variability in Denmark Strait and its influence on overflow water. *J. Phys. Oceanogr.* 49:1889–904
Sullivan PP, McWilliams JC. 2018. Frontogenesis and frontal arrest for a dense filament in the oceanic surface boundary layer. *J. Fluid Mech.* 837:341–80

Sullivan PP, McWilliams JC. 2019. Langmuir turbulence and filament frontogenesis in the oceanic surface boundary layer. *J. Fluid Mech.* 879:512–53

Sullivan PP, McWilliams JC, Weil JC, Patton EG, Fernando HJS. 2020. Marine boundary layers above heterogeneous SST: across-front winds. *J. Atmos. Sci.* In press. **https://doi.org/10.1175/JAS-D-20-0062.1**

Suzuki N, Fox-Kemper B, Hamlington PE, Van Roekel LP. 2016. Surface waves affect frontogenesis. *J. Geophys. Res. Oceans* 121:3597–624

Taylor JR, Ferrari R. 2009. On the equilibration of a symmetrically unstable front via a secondary shear instability. *J. Fluid Mech.* 622:103–13

Thomas LN. 2008. Formation of intrathermocline eddies at ocean fronts by wind-driven destruction of potential vorticity. *Dyn. Atmos. Oceans* 45:252–73

Thomas LN. 2017. On the modifications of near-inertial waves at fronts: implications for energy transfer across scales. *Ocean Dyn.* 67:1335–50

Thomas LN, Lee C. 2005. Intensification of ocean fronts by downfront winds. *J. Phys. Oceanogr.* 35:1086–102

Thompson LN. 2000. Ekman layers and two-dimensional frontogenesis in the upper ocean. *J. Geophys. Res.* 105:6437–51

Tintore J, La Violette PE, Blade I, Cruzado A. 1988. A study of an intense density front in the Eastern Alboran Sea: the Almeria-Oran front. *J. Phys. Oceanogr.* 18:1384–97

Ungarish M, Huppert HE. 1998. The effects of rotation on axisymmetric gravity currents. *J. Fluid Mech.* 362:17–51

van Heijst GJF. 1986. On the dynamics of a tidal mixing front. In *Marine Interfaces Ecohydrodynamics*, ed. JCJ Nihoul, pp. 165–94. Amsterdam: Elsevier

Verma V, Pham HT, Sarkar S. 2019. The submesoscale, the finescale and their interaction at a mixed layer front. *Ocean Model.* 140:101400

Wang DP, Jordi A. 2011. Surface frontogenesis and thermohaline intrusion in a shelfbreak front. *Ocean Model.* 38:161–70

Annual Review of Marine Science

Volume 13, 2021

Contents

Errata

An online log of corrections to *Annual Review of Marine Science* articles may be found at http://www.annualreviews.org/errata/marine